

Weierstraß-Institut
für Angewandte Analysis und Stochastik
Leibniz-Institut im Forschungsverbund Berlin e. V.

Preprint

ISSN 2198-5855

Influence of cell shape, inhomogeneities and diffusion barriers
in cell polarization models

Wolfgang Giese¹, Martin Eigel², Sebastian Westerheide³,

Christian Engwer³, Edda Klipp¹

submitted: June 3, 2014

¹ Theoretical Biophysics
Humboldt-Universität zu Berlin
Theoretical Biophysics
Invalidenstr. 42
10115 Berlin
E-Mail: wolfgang.giese@biologie.hu-berlin.de
edda.klipp@rz.hu-berlin.de

² Weierstrass Institute
Mohrenstr. 39
10117 Berlin
Germany
E-Mail: martin.eigel@wias-berlin.de

³ Institute for Computational und Applied Mathematics
University of Münster
Orleans-Ring 10
48149 Münster
Germany
E-Mail: sebastian.westerheide@uni-muenster.de
christian.engwer@uni-muenster.de

No. 1959
Berlin 2014



2010 *Mathematics Subject Classification.* 35Q92, 92C37, 65M60, 74S05, 92-08, 37N25, 46N60, 62P10, 92C45, 97M60.

Key words and phrases. Polarization models, surface FEM, bulk-surface PDE, computer simulation, spatial simulation, spatial inhomogeneities, Cdc42.

This work was supported by a grant from the German Research Foundation through CRC 740 "From molecules to modules" to EK.

Edited by
Weierstraß-Institut für Angewandte Analysis und Stochastik (WIAS)
Leibniz-Institut im Forschungsverbund Berlin e. V.
Mohrenstraße 39
10117 Berlin
Germany

Fax: +49 30 20372-303
E-Mail: preprint@wias-berlin.de
World Wide Web: <http://www.wias-berlin.de/>

INTRODUCTION

Fundamental processes of living cells such as cell division, chemotaxis and morphogenesis depend on a prior polarization and spatial symmetry break. In these processes, cells have to adapt and react according to multiple, often conflicting cues of the environment. Spatial reorganization of membrane-bound and cytosolic proteins are needed to establish an axis of polarity with a distinct direction (i.e. “front and back”) to guide directed processes. Advances in fluorescence imaging techniques have enabled insights into the spatial distribution of molecules that initiate the symmetry break necessary for cell polarization. However, the extensive efforts of experimentalists have to be complemented by mathematical models describing the observed behaviour. Only then a true understanding of the underlying mechanisms can be achieved.

The theoretical treatment of cell polarization has been devoted to biological model organisms as yeast, fish karyotes, *Dictyostelium* or neutrophils. Much recent work is concerned with reaction-diffusion (RD) models which are often described by partial differential equations (PDEs) in time and space as in [34, 30, 44, 43, 1, 37, 21, 9, 42]. These models are of varying complexity. Some of them are based on biochemical networks [9, 21] gathered from pathway databases, while others focus on a few components to accurately describe observed behaviour. Detailed reviews of models for yeast cell polarity can be found in [23, 36].

These two approaches pursue different goals. Since biochemical complexity can become overwhelmingly large, the experimental validation of such generated models of high complexity is basically impossible [25, 24] and an accurate spatial simulation becomes prohibitively costly. The alternative is the reduction of signaling pathways to very few interacting constituents which still exhibit the specific behaviour one is interested in. This simplified model can then be simulated with a spatio-temporal mathematical model which also includes (some) geometrical properties encountered in living cells. Ideally, observed in vivo or in vitro phenomena can be reconstructed, rates and concentrations can be compared and matched.

While recent advances in imaging techniques such as total internal reflection fluorescence (TIRF) and confocal and electron microscopy have the potential to also provide quantitative data of the considered process [2, 29, 53, 28], computer simulations based on such models most often are restricted to severely limited settings. In particular, computations are usually carried out in just one dimension (instead of 2 or 3), the interaction of cytosolic (volume) and membrane (surface) constituents is simplified, and inhomogeneities of the involved media is neglected. Since the diffusion of membrane-bound molecules is much slower than the diffusion of cytosolic molecules, the diffusion in the cytosol is often considered to be instantaneous for model simplification [21, 1, 19].

However, in [35, 39] it has been shown that high intracellular cytosolic gradients can be generated. Even though diffusion in the cytosol might be fast in theory, it can differ a lot from the effective diffusion rate when obstacles like large organelles, membrane structures or a crowded environment are considered [47]. Therefore, it is important to incorporate diffusion and intracellular gradients in the cytosol [17, 11, 49].

In comparison to the cytosol, the cell membrane is a thin layer which allows diffusion only in lateral direction [48]. Moreover, membrane curvature has to be represented properly which can only be done in 2D or in 3D. While some models [40, 33] show that membrane curvature and shape can influence signaling, none of the models known to us has addressed inhomogeneities in the diffusion process that can occur on the membrane, e.g. bud scars in yeast or hindered diffusion in the cytosol, caused e.g. by organelles. However, membrane inhomogeneities are in fact likely to have an effect on signaling [51].

Therefore, we present an advanced computational approach which takes into account some important aspects of spatial complexity in order to assess its influence in the examined models. It is determined by the cell shape, cell size and spatial inhomogeneities. The membrane is modeled as a surface in 2D or 3D space where the enclosed volume represents the cytosol, see Figure 1. The RD model equations connect membrane and cytosol by kinetic coupling terms which depend on the concentration of membrane-bound and cytosolic species. Spatial inhomogeneities as organelles or bud scars can be represented by an inhomogeneous diffusion coefficient or as inner boundaries in the computational domain. Our computational approach relates to recent advances in surface finite element methods (SFEM) [15, 40] which also take into account surface curvature of the membranes. With these methods the RD model equations can be solved with high accuracy and great flexibility regarding the spatial geometry.

One prominent example for cell polarization is the yeast budding process where inactive cytosolic Cdc42 is recruited to the membrane and amplified via its GEF Cdc24 and by the effector Bem1. Additionally it can be deactivated and dissolved from the membrane to the cytosol by its GAP. In the course of these interactions, a unique polarization cap of active Cdc42 is generated on the cell membrane which initiates the emerging bud on the site of the polarization cap [42]. A sketch of this process is shown in Figure 1.

In this article, we consider two common mechanisms for cell polarization that involve an active membrane-bound and an inactive cytosolic species. The first of these mechanisms is of Turing-type [43, 21]. In this case the system starts in a homogeneous steady state which is unstable with respect to minute spatial perturbations and runs into a spatially inhomogeneous polarized state. The second is a Wave-Pinning mechanisms [37, 52]. Here, the corresponding homogeneous system has two stable and one unstable transient steady state. The steady state at lower concentration of active membrane-bound molecules corresponds to an unexcited state, the steady state at higher surface concentration corresponds to an excited state. Stimulation of the system causes travelling waves on the cell surface that are pinned into a polar stable state due to global mass conservation.

Our main intention is to examine and illustrate the importance of spatial properties when considering such models. These are e.g. the cell shape, cell size and the location of (large) organelles in the cytosol by which the polarization location and strength is distinctly influenced. We also demonstrate the interplay of competing stimuli in our *in silico* experiments.

RESULTS

A two component model for cell polarization. In the geometric representation of the cell we incorporate the cell membrane, the cytosol and inner membranes that enclose organelles like the vacuole or the nucleus. We assume free diffusion of molecules in the cytosol which is limited by the outer boundary of the cell and the inner membranes of the organelles. The cytosolic volume is denoted by V^{cyt} and its boundary surface is $\partial V^{\text{cyt}} = M^{\text{cell}} \cup M^{\text{org}}$ consisting of the outer cell membrane M^{cell} and the membranes of contained organelles M^{org} (see Figure S1) with $M^{\text{org}} = \partial N \cup \partial V$. Here, ∂D denotes the boundary of some domain D . The active membrane-bound form of the signaling molecule is represented by its concentration $u(\vec{x}, t)$ and the inactive cytosolic form is represented by its concentration $v(\vec{x}, t)$. These are both functions of space, $\vec{x} \in M^{\text{cell}} \subset \mathbb{R}^d$ respectively $\vec{x} \in V^{\text{cyt}} \subset \mathbb{R}^d$ ($d = 2, 3$), and time $t \in [0, T]$ with end time T . With this geometric representation of the cell, the shuttling between membrane-bound and cytosolic signaling molecules are naturally described by a flux $J = f(u, v)$ at the membrane-cytosolic interface, which follows a specific kinetic depending on

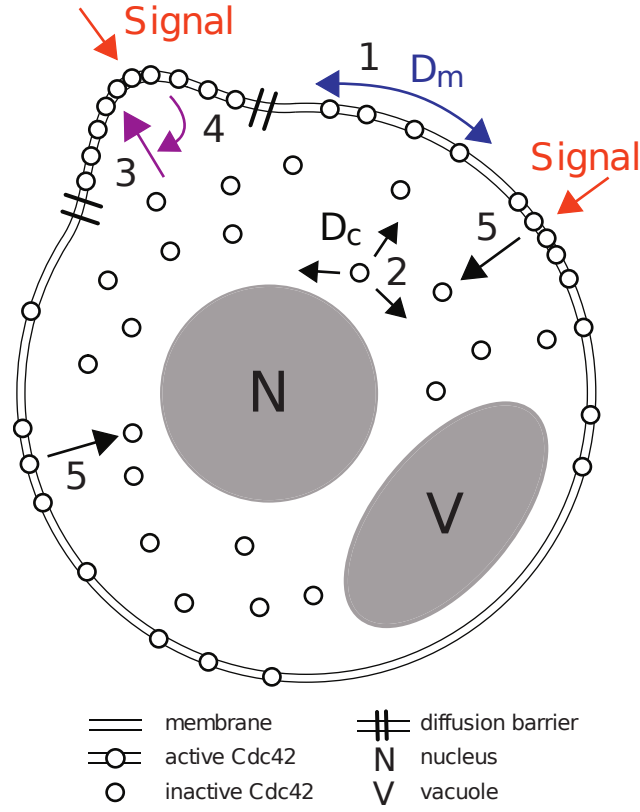


FIGURE 1. A scheme of the cycling process of signaling molecules between cytosol and membrane: (1) lateral diffusion with coefficient D_m of active signaling molecules along the membrane; (2) free cytosolic diffusion with coefficient D_c of inactive signaling molecules; (3) association of cytoplasmic molecules to the membrane; (4) positive feedback, i.e. enhanced recruitment of cytoplasmic molecules to the location of active signaling molecules; (5) dissociation of signaling molecules from the membrane.

concentrations u and v . The model is formulated as the system of partial differential equations

$$(1) \quad \frac{\partial u}{\partial t} = \nabla_{\Gamma} \cdot (D_m \nabla_{\Gamma} u) + f(u, v) + k_S v \quad \text{on } M^{\text{cell}},$$

$$(2) \quad \frac{\partial v}{\partial t} = \nabla \cdot (D_c \nabla v) \quad \text{in } V^{\text{cyt}},$$

with boundary conditions

$$(3) \quad -D_c \nabla v \cdot \vec{n} = f(u, v) + k_S v \quad \text{on } M^{\text{cell}},$$

$$(4) \quad -D_c \nabla v \cdot \vec{n} = 0 \quad \text{on } M^{\text{org}}.$$

Moreover, the initial concentrations at time $t = 0$ are given by

$$(5) \quad u(\vec{x}, 0) = u_0(\vec{x}) \quad \text{and} \quad v(\vec{x}, 0) = v_0(\vec{x}).$$

These equations comprise three types of processes which occur simultaneously: **(a)** Diffusion of $u(\vec{x}, t)$ on the curved membrane where the diffusion coefficient $D_m(\vec{x})$ is a function in space in order to allow inhomogeneous diffusion and ∇_{Γ} denotes the surface gradient operator in \vec{x} which accounts for curvature of Γ , see [15]. **(b)** Diffusion of $v(\vec{x}, t)$ in the cytosol with diffusion coefficient $D_c(\vec{x})$ and ∇ denotes the gradient operator in \vec{x} . **(c)** Reaction processes on the membrane are described by a source term $f(u, v)$ for the membrane-bound complex in equation (1). They are modeled as a Robin-like boundary conditions for the cytosolic concentration $v(\vec{x}, t)$ in equation (3). The cytosolic species v only interacts with the membrane-bound species u on the cell membrane M^{cell} . Hence, there is no

extra reaction term in the volume equation (2). For $f(u, v) > 0$ we have a flux from the cytosol to the membrane, whereas for $f(u, v) < 0$ the active form u dissociates into the cytosol. The function $k_S(\vec{x}, t)$ depends on space and time and accounts for signals that excite the system and cause a flux from cytosol to membrane, e.g. spontaneous activation of some signaling molecule. This equation system is mass conservative which means that the total mass of the considered signaling molecule is constant in time, i.e. (see Supporting Text for the derivation)

$$\underbrace{\int_{M^{\text{cell}}} u \, dA}_{\text{mass on the cell membrane}} + \underbrace{\int_{V^{\text{cyt}}} v \, dV}_{\text{mass in the cytosol}} \equiv K \in \mathbb{R}.$$

The model is applicable with 2D and 3D representations of the cell. Like in reality the membranes are 2D surfaces which enclose a 3D volume. Moreover, the model can also be used to describe processes in a thin slice of the cell. In this dimension reduced case, the cytosol is a domain in the 2D plane describing the considered slice and the membrane is a 1D curve representing the boundary of this planar domain. Figure 2 gives an overview of the different representations and the respective units and ratios between volume and surface domains.

In the general framework for cell polarization models, the flux/source term $f(u, v)$ incorporates a self-amplifying feedback on the active membrane-bound species u . The location where most active signaling molecules are accumulated also recruits the most inactive signaling molecules from the cytosol. This has to be understood as a competition between different polarization sites since the cytosolic pool of inactive cytosolic molecules is limited. There are several different model realizations for $f(u, v)$ with different properties [1, 37, 43, 21]. We investigate two conceptual models, the GOR model from Goryachev et al. [21] and the wave-pinning WP model from Mori et al. [37]. The GOR model [23, 21, 42] represents a Turing-type mechanism and is derived as a simplification of a detailed biochemical signaling pathway involved in the yeast budding process. It employs the kinetics

$$(6) \quad f(u, v) = f_{\text{GOR}}(u, v) = \alpha E_c u^2 v + \beta E_c u v - \gamma u.$$

Here, α , β and γ are constants and we choose the parameter values $\alpha = 0.0033$, $\beta = 0.0067$, $\gamma = 0.017$ as in [21]. E_c accounts for the *Bem1-Cdc42* complex and is taken to be constant for simplicity. The reaction kinetics $f_{\text{GOR}}(u, v)$ is plotted in Figure S2 (see Supporting Text) for fixed values of v . We choose $u_0(x) \equiv 0.6$ and $v_0(\vec{x}) \equiv 2.0$ as initial conditions for the GOR model throughout this paper, which corresponds to the non-zero homogeneous steady state of the system. The WP model with flux/source term

$$(7) \quad f(u, v) = f_{\text{WP}}(u, v) = v \left(k_0 + \frac{\gamma u^2}{K^2 + u^2} \right) - \delta u$$

was thoroughly investigated in [23, 37, 38, 52]. The reaction kinetics of $f_{\text{WP}}(u, v)$ is also plotted in Figure S2 for fixed values of v , where $k_0 = 0.067$, $\delta = 1$, $\gamma = 1$ and $K = 1$ are the corresponding parameter values. In all experiments shown in this paper, we use $u_0(\vec{x}) \equiv 0.2$ and $v_0(\vec{x}) \equiv 1.95$ as initial conditions for the WP model, which corresponds to the stable unexcited homogeneous steady state of the system.

In the original works [37], [21] different values for the diffusion coefficients are used, even though both refer to measured values in the model organism yeast. The diffusion coefficients $D_c = 10.0 \mu\text{m}^2/\text{s}$ in the cytosol and $D_m = 0.1 \mu\text{m}^2/\text{s}$ on the membrane are used for the WP model, while $D_c = 1.0 \mu\text{m}^2/\text{s}$ and $D_m = 0.0025 \mu\text{m}^2/\text{s}$ are used for the GOR model. Therefore, the diffusion coefficient on the membrane varies about a factor of 40. These discrepancies can still be found in recent literature. For instance in [42] a value of $D_m = 0.0025 \mu\text{m}^2/\text{s}$ is used, while in [19] a 15-fold larger value of $D_m = 0.037 \mu\text{m}^2/\text{s}$ is employed for the model organism yeast. It is not the aim of this work to resolve these conflicts, but to show that despite these discrepancies of parameters the behaviour of both

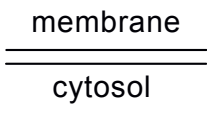
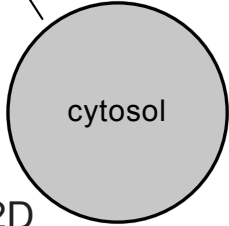
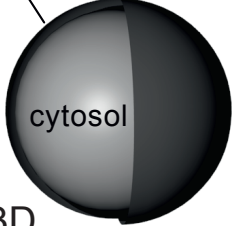
	<div style="text-align: center;">  </div> 1D	<div style="text-align: center;">  </div> 2D	<div style="text-align: center;">  </div> 3D
representation of cytosol	line	area	volume
representation of membrane	line	curve	surface
cytosolic conc.	$\text{mol } \mu\text{m}^{-3}$	$\text{mol } \mu\text{m}^{-3}$	$\text{mol } \mu\text{m}^{-3}$
membrane conc.	$\text{mol } \mu\text{m}^{-3}$	$\text{mol } \mu\text{m}^{-2}$	$\text{mol } \mu\text{m}^{-2}$
flux $J = f(u,v)$	$\text{mol } \mu\text{m}^{-3} \text{ s}^{-1}$	$\text{mol } \mu\text{m}^{-2} \text{ s}^{-1}$	$\text{mol } \mu\text{m}^{-2} \text{ s}^{-1}$
surface/ volume ratio	1	$2 / R$	$3 / R$

FIGURE 2. Conceptual representations of the cell and its outer membrane in different dimensions (1,2,3). In the 1D model, both membrane and cytosol are modeled as the same interval on the real axis, which represents a cell diameter transect. In 2D and 3D, the whole cell can be represented with a more realistic shape. The membrane then is modeled as a thin layer around the domain which only allows lateral diffusion. As a consequence, also the units for fluxes and reaction rates on the membrane and in the volume have different units.

models can be dramatically influenced by cell shape and diffusion inhomogeneities. Therefore, we also simulated both models with consensus parameters, $D_c = 3.0 \mu\text{m}^2/\text{s}$ and $D_m = 0.015 \mu\text{m}^2/\text{s}$, which are approximately the geometric mean of the extreme values for the diffusion coefficients.

To qualitatively compare the influence of different spatial effects, both models are excited and probed with stimuli of the form

$$(8) \quad k_S(\vec{x}, t) = \begin{cases} S_1, & \text{if } t < t_1 \text{ and } \text{dist}(\vec{x}_{S_1}, \vec{x}) < R, \\ S_2, & \text{if } t < t_2 \text{ and } \text{dist}(\vec{x}_{S_2}, \vec{x}) < R, \\ 0, & \text{otherwise,} \end{cases}$$

for all shown experiments. Here, $\text{dist}(\vec{x}_1, \vec{x}_2)$ denotes the distance between \vec{x}_1 and \vec{x}_2 and R specifies the excited surface area. In general, we excite the system with two different competing signals at positions \vec{x}_{S_1} and \vec{x}_{S_2} on the cell membrane, where each signal covers 5% of the cell surface. We set different amplitudes for both stimuli which are $S_1 = 0.44$ and $S_2 = 0.4$. Therefore, S_1 is 10% stronger than S_2 to produce a bias towards the stimulus S_1 in the initial phase of cell polarization. Both stimuli are applied for a time period of $\Delta t = 10\text{s}$. It shall be noted that the subsequent results could also qualitatively be achieved by varying the duration of the stimuli, e.g. setting $S_1 = S_2$ but applying the stimulus at \vec{x}_{S_1} for $\Delta t = 12\text{s}$ and the stimulus at \vec{x}_{S_2} for $\Delta t = 10\text{s}$.

The main focus of this work is to investigate how the geometry of the cell and how spatial inhomogeneities influence the polarization behaviour for the two considered polarization models. More specifically, we examine in detail how cell shape, cell size and diffusion barriers on the membrane and in the cytosol influence the outcome (i.e. the formation of a cluster) of the competition among two different polarization locations. We perform a vast number of computational experiments in order to assess the qualitative dependence of the simulation results on these parameters. Since the models

are conceptual and lack biochemical and quantitative details on the reaction kinetics, we restrict ourselves to computations in 2D which also makes the discussed results more accessible to an intuitive understanding of the observed effects. Assuming circular cells with radius R , the ratio of surface to volume is $2/R$ whereas in 3D it is $3/R$ (see Figure 2). Hence, in 2D and 3D the surface to volume ratio scales reciprocal to the cell radius which is in contrast to the 1D setting. Principally, all kinds of inhomogeneities and asymmetries in cells such as diffusion barriers and different cell shapes can already be studied in 2D to a large extent and conclusions typically can be transferred to the 3D case. Apart from being more complex to comprehend, setup and reproduce, 3D simulations are also computationally very costly while they would add only little benefit to conceptual qualitative studies as carried out in this article. For both models GOR and WP we could qualitatively reproduce the 1D simulations performed in the review article [23]. A comparison of 1D and 2D simulations for the GOR and the WP model with two competing stimuli can be found in Figure S3 in the Supporting Text.

(A) Cell protrusion acts as a negative feedback on cluster formation. In the first setup we thrive to understand the influence of the cell shape on the polarization behaviour by the introduction of a small geometry perturbation to an otherwise fully circular cell. It has been shown in [35] that the cell shape potentially influences signaling within the cell for one cytosolic species, neglecting the membrane-cytosol shuttling. Moreover, rapid cell shape changes of fast moving neutrophil cells [40, 22] can affect the distribution of signaling molecules. However, for a feedback model with the interplay of slow membrane and fast cytosolic diffusion, the effect to expect is not obvious.

In the following experiments we incorporate a small protrusion into a circular cell as shown in Figure 3. The two stimuli $S1$ and $S2$ introduced in equation (8) are imposed on the cell surface. The stronger stimulus $S1$ is located at the protrusion while the weaker stimulus $S2$ is located on the right-hand side center of the cell. The protrusion length is varied from $-0.5\mu m$ to $2\mu m$. As a matter of fact, for the negative value $-0.5\mu m$ we obtain an intrusion and for the value $0.0\mu m$ the circular cell is unperturbed, see Figure 3B.

The GOR model is simulated with the diffusion coefficients from the original work [21], which are $D_c = 1\mu m^2/s$ and $D_m = 0.0025\mu m^2/s$ and the consensus diffusion coefficients $D_c = 3\mu m^2/s$ and $D_m = 0.015\mu m^2/s$ for comparison. For the circular cell we observe the expected outcome: the stronger stimulus $S1$ induces a cluster of active membrane-bound molecules which dominates the smaller cluster induced by $S2$. Eventually, the smaller cluster vanishes and the system reaches steady state. However, we observe that already a small protrusion reverses the outcome, see Figure 3B on the right. On the one hand, the protrusion causes a negative feedback on signal $S1$. On the other hand, an intrusion causes a positive feedback on $S1$ and the polarization is established even faster than in the case of a fully circular shape.

For the WP model, in principle the same qualitative behaviour is observed. Again we use the diffusion coefficients $D_c = 10\mu m^2/s$ and $D_m = 0.1\mu m^2/s$ from the original work [38] for comparison with the consensus values $D_c = 3\mu m^2/s$ and $D_m = 0.015\mu m^2/s$. For the fast diffusion coefficients $D_c = 10\mu m^2/s$ and $D_m = 0.1\mu m^2/s$ we observe a travelling wave on the membrane, where finally both clusters merge into a single one. This can be observed for a protrusion length smaller than $1.5\mu m$. For a protrusion length larger than $1.5\mu m$, the cluster at $S1$ vanishes. Interestingly, with the intrusion both clusters merge and the center of the induced travelling wave moves slowly towards the intrusion. For the slower diffusion coefficients $D_c = 3\mu m^2/s$ and $D_m = 0.015\mu m^2/s$, the two clusters at $S1$ and $S2$ do not merge and the system is even more sensitive with respect to the shape.

To complete the shape related experiments, we also investigate the influence of the protrusion width. The protrusion length is fixed at $1.0\mu m$ and the width varies from $1.0\mu m$ to $3.5\mu m$, see Figure 3C. Note that a width of $1.5\mu m$ corresponds to the shape with a protrusion length of $1\mu m$ in Figure 3B. For the GOR model we observe a shift in the qualitative outcome at a width of $3.0\mu m$ for $D_c = 1\mu m^2/s$

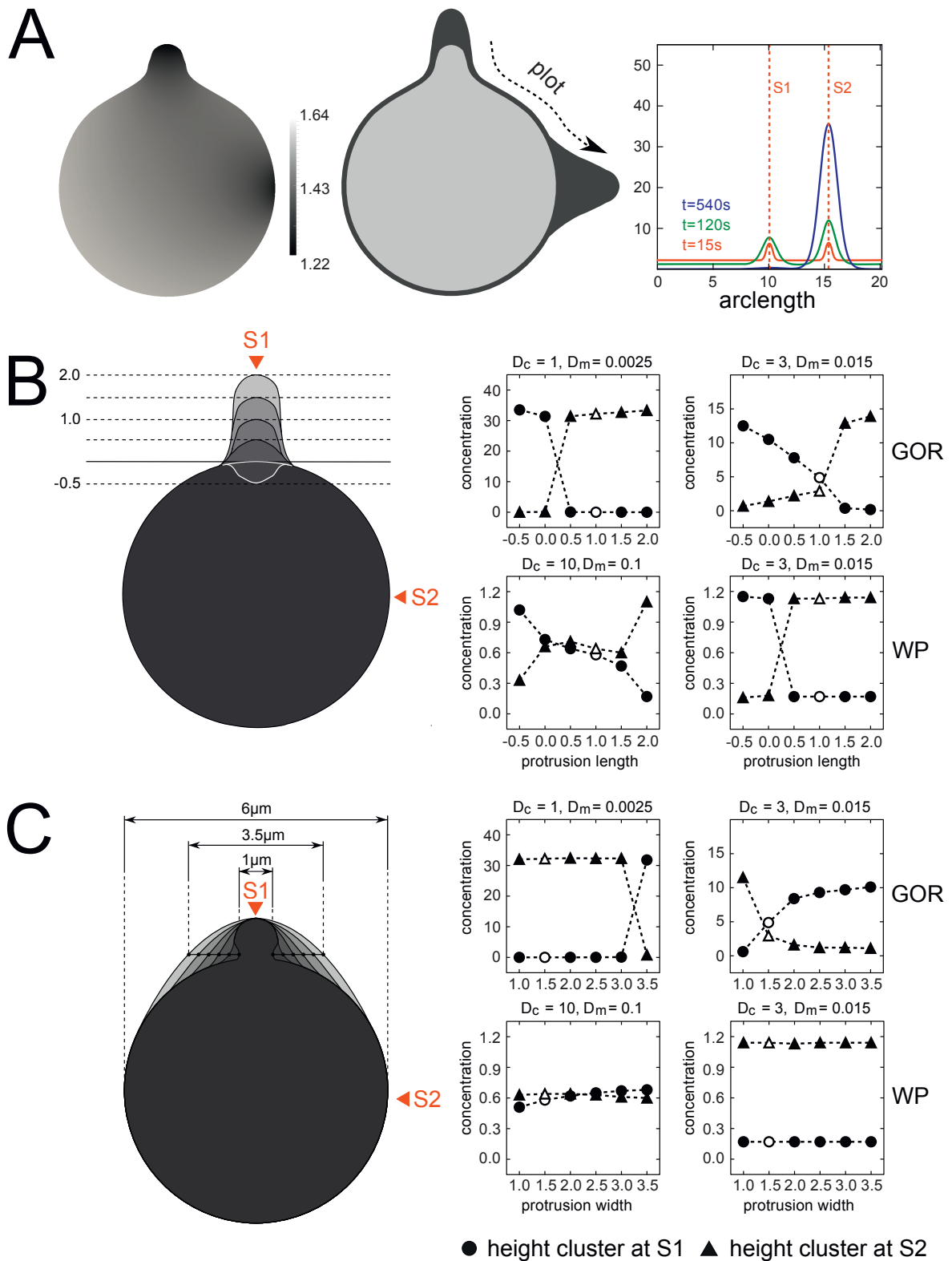


FIGURE 3. (A) The GOR model is simulated for a cell with a protrusion and two competing stimuli S_1 and S_2 . The cytosolic distribution [left] is shown at time $T = 120s$. The concentration distribution is plotted along the circumference of the cell [middle]. From this distribution an arclength plot is derived for different times [right]. (B) Varying the length of the cell protrusion has an influence on the cluster formation. The height of the clusters at S_1 and S_2 is plotted at steady for the GOR and the WP model with different diffusion coefficients. (C) For the same setup the width of the protrusion is varied. The outcome is plotted on the right. Note that the empty symbols mark the cell shape that occurs both in (B) as well as in (C).

and $D_m = 0.0025\mu\text{m}^2/s$. The effect of the wider protrusion is less pronounced and the stronger stimulus $S1$ dominates the polarization process. We thus get the same qualitative outcome as for the circular case. The WP model exhibits a more robust behaviour against changes of the protrusion width. For both tested diffusion coefficients, the qualitative outcome stays the same.

The effect that we observe in the simulations can be described as a kind of "bottle neck" caused by the perturbation at the signal site $S1$. In particular, diffusive transport into the protrusion is slightly hindered when compared to diffusion to the unperturbed membrane. Thus, the location with the stronger stimulus $S1$ at the protrusion is not able to "win the competition" against the initially smaller cluster at $S2$ due to insufficient transport of inactive signaling molecules to the binding site at $S1$.

This demonstrates nicely that small perturbations in the cell shape may lead to a qualitative difference in the behaviour of both models. One interpretation of this observation is that the growth of a protrusion evokes a direct feedback on the underlying biochemical process, i.e. spatial geometrical changes cause changes in the biochemical properties of signaling pathways.

(B) There is an optimal cell size for polarization. In the previous experiments in (A), we simulate a cell with constant diameter $6\mu\text{m}$. A variation of the cell's diameter directly determines the distances that molecules have to travel within the cell. For instance, the mean square displacement for a molecule in some time interval Δt in the cytosol can be calculated from $D_c\Delta t$. Assuming the diffusion coefficient in the range $1\mu\text{m}^2/s - 10\mu\text{m}^2/s$ [21, 23, 7], we can conclude that the mean free path per second $\sqrt{D_c\Delta t}$ varies between $1\mu\text{m} - 3.16\mu\text{m}$. For a small cell with a diameter of $3\mu\text{m}$, which can be assumed for small yeast cells, this means that one molecule typically travels from one end of the cell to the other in less than one second. It thus is apparent that passive transport processes in small cells are much more efficient than in larger volumes.

Changing the cell size by a scaling factor $\xi > 0$ can be achieved in the simulation by a transformation of variables $\vec{x} = \xi\vec{x}$. For the formulation and solution of the model equations, we observe that scaling the domain size by ξ is equivalent to changing the diffusion coefficients to $\tilde{D}_c = D_c/\xi^2$ and $\tilde{D}_m = D_m/\xi^2$ where the superscript tilde denotes the scaled quantities. Furthermore the boundary condition (3) has to be rescaled as follows:

$$(9) \quad \tilde{D}_c \nabla v \cdot \vec{n} = \frac{1}{\xi} f(u, v) + \frac{1}{\xi} k_S v.$$

Simulations for circular cells with cell diameters in the range of one order of magnitude from $1.5\mu\text{m}$ up to $15\mu\text{m}$ are performed to illustrate this effect. For all cell sizes, we again impose two stimuli $S1$ and $S2$ at two different locations on the cell membrane. The amplitudes of the stimuli are fixed while the membrane areas of the stimuli applications are scaled proportionally to the cell size to make simulations with different diameters comparable. In general, two clusters emerge and compete with each another. It is then of interest which influence the cell's diameter has on this competition.

We use two measures to compare the degree of polarization on the membrane (see Methods section). The first is the mean polarization (POL) which relates the highest concentration to the total mean concentration on the surface normalized by the surface area. The second is the polarization factor (PF) which is calculated from the area of the smallest surface patch that comprises half of the mass on the surface. For the steady states of the simulations, we calculate PF and POL for varying cell sizes, see Figure 4.

The GOR and WP models exhibit essentially different polarization behaviours. For the GOR model the clusters grow mainly in "height" (i.e. locally high concentrations), while for the WP model a travelling wave can be observed where the cluster grows in width but not in height.

For the GOR model we observe that the POL measure is slightly decreasing, since the cluster height does not grow proportionally to the cell size (compare Figure 4). On the other hand the relative cluster

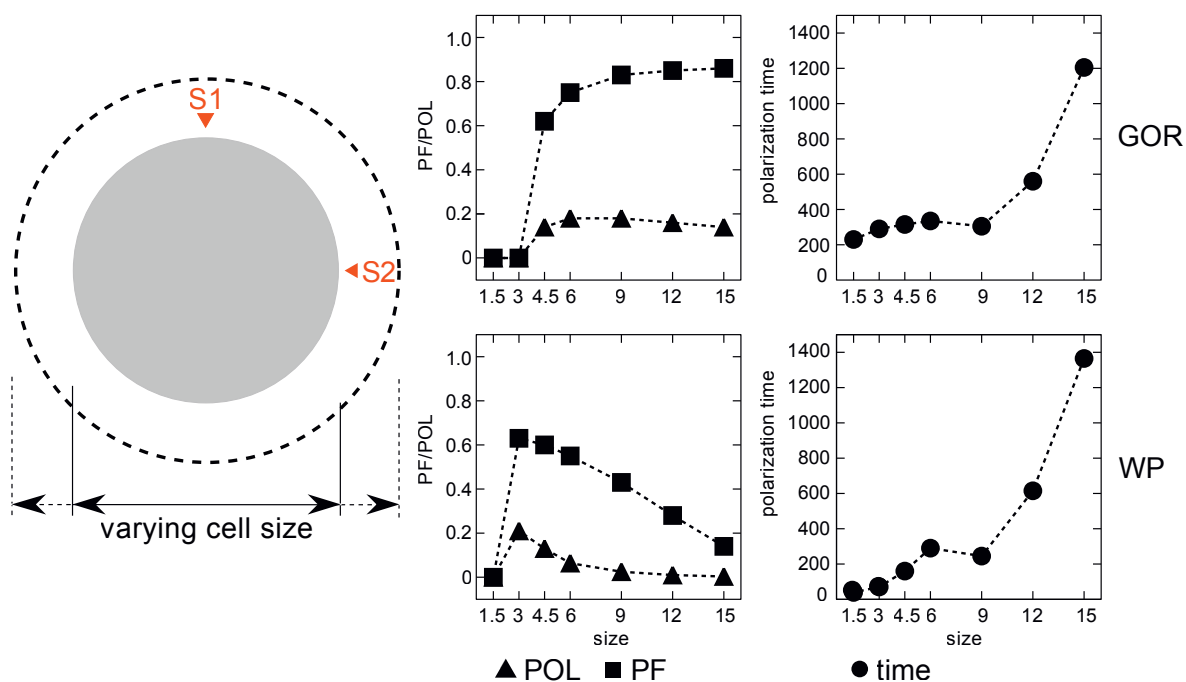


FIGURE 4. The maxima of the polarization measures PF and POL are plotted for different cell sizes [center column], see results section (B). Moreover, the polarization time, i.e. the time when 90% of the maximal (PF) value is reached, is shown [right column].

width is decreasing and therefore the PF measure is increasing with cell size. The development of the relative cluster width in relation to the cell size is shown in Figure S5 in the Supporting Text. It shall be noted that for a cell size smaller than $4.5\mu m$, polarization is not achieved for the employed parameters.

For the WP model the POL measure decreases with larger cells since the cluster height is the same for smaller and larger cell shapes. The PF measure decreases as well. The surface to volume ratio scales with $2/R$. Hence, if the maximum concentration of the cluster is fixed, the cluster width grows with the cell size. An explicit formula of the cluster width is derived in the Supporting Text. The formula is in almost exact agreement with the numerical 2D simulation and predicts that the relative cluster grows linearly with R . For a cell size of $R = 15\mu m$ more than 80% of the cell surface is polarized (see Figure S5 in the Supporting Text). For a cell size smaller than $3\mu m$, polarization is not achieved.

We also compare the duration for the build-up of polarization by measuring the time until 90% of the final PF value is reached. Especially the increase for larger cells is significant. In fact, the polarization time for a cell with diameter of $15\mu m$ is almost four times higher than that for a cell of diameter $6\mu m$.

For both models we observe that polarization is either not possible for very small cells or takes very long for larger cells. For the chosen parameter values, we can demonstrate that there is indeed an optimal cell size for both examined mechanisms. For the considered models the optimal cell size lies in between $5\mu m$ and $10\mu m$.

(C) Membrane barriers can amplify cluster formation. Interior subdomains such as organelles and diffusion barriers on the membrane potentially play an important role in the signaling process. In the budding yeast, bud and birth scars occur after cell division and may have an influence on subsequent cell polarization. Furthermore, it is known that during cell division diffusion barriers are established to separate material of mother and daughter cells still sharing a contiguous membrane [8]. In a recent study [42] it is shown that septin structures in yeast are formed in the early phase of polarization

and that Cdc42 clusters can be trapped in these regions. We introduce membrane diffusion barriers into the model to examine the influence of these inhomogeneities on the polarization behaviour, see Figure 5.

As in the previous setups, two signals $S1$ and $S2$ of different strengths are applied but their positions are switched (see Figure 5). Therefore, the weaker stimulus $S1$ is located at the protrusion to demonstrate the strong influence of diffusion barriers on the membrane. First, we simulate the effect of diffusion barriers surrounding the location of signal $S1$ (see Figure 5 left column). For both models we use again the diffusion coefficients $D_c = 3\mu\text{m}^2/\text{s}$ and $D_m = 0.015\mu\text{m}^2/\text{s}$ and a cell with a protrusion of length $1.5\mu\text{m}$, which is exactly the same cell geometry as used in section (A). In contrast to section (A) the weaker stimulus is applied at the protrusion $S1$. However, this time it is surrounded by diffusion barriers. Interestingly, the cluster induced by the weaker stimulus $S1$ now grows steadily while the cluster induced from the stronger stimulus $S2$ vanishes. Hence, the diffusion barriers compensate the negative feedback caused by the protrusion as examined in (A). This effect can be observed for both models. The result is shown in Figure 5 left column. The observed effect can be attributed to an easier accumulation of signaling molecules at $S1$ since the transport away from $S1$ is blocked by the introduced barriers.

We repeat the same setup with the same parameters and cell shapes. However, this time we employ a one-sided diffusion barrier which is placed next to signal $S1$ at the protrusion, see Figure 5 right column. In yeast cells, such impermeable regions on the membrane could correspond to bud scars which emerge after cell division. It is a topic of current research to find out whether these scars have an influence on the budding process. For the GOR model, we observe that due to restricted diffusion caused by the barrier, the cluster at the weaker stimulus $S1$ grows much stronger than the cluster at the stronger stimulus $S2$. We thus have the same effect as for surrounding diffusion barriers. However, the influence of a one-sided diffusion barrier is weaker and can not compensate the negative feedback induced by the protrusion in the case of the WP model.

The effects of barriers surrounding the protrusion and impermeable regions in the vicinity of the signal are qualitatively similar. During cluster formation on the membrane, active membrane-bound molecules diffuse laterally from high concentrations to low concentrations with diffusion coefficient D_m . Reducing this diffusion diminishes the diffusive flux which counteracts the growth of the cluster. Therefore, diffusion barriers on the membrane have the potential to accelerate and stabilize cell polarization.

(D) Organelles in the cytosol can alter polarization preferences. Cells accommodate many structures of different sizes, for instance large membrane structures like the endoplasmic reticulum, the nucleus and other organelles. Thanks to recent advances in imaging technologies, very detailed microscopic images of the cytoplasm can be produced, see for example [29, 54]. Intracellular structures certainly influence diffusive but also vesicular transport in the cell [32, 17, 5]. During cell division, the spatial position of the organelles has to be organized and is most likely controlled by signaling, but effectively also influences signaling itself. Even for small cells, the calculation of effective diffusion coefficients is usually inferred from molecule properties and viscosity of the medium. However, these derivations do not incorporate intracellular diffusion barriers as organelles or impermeable membranes in general. Therefore, we examine which effects obstacles in the medium have on intracellular gradients.

To address this goal, we perform computational experiments with organelles of different sizes and shapes placed in different areas of a circular cell, see Figure 6. As in the setups before, two competing signals $S1$ and $S2$ are applied. For both models we again use the diffusion coefficients $D_c = 3\mu\text{m}^2/\text{s}$ and $D_m = 0.015\mu\text{m}^2/\text{s}$. During initial growth and competition of the two clusters, the cytosolic concentration decreases in between the large organelle and the membrane at the stronger signal $S1$. Since cytosolic transport is limited in the vicinity of $S1$ due to the obstacle and inactive signaling

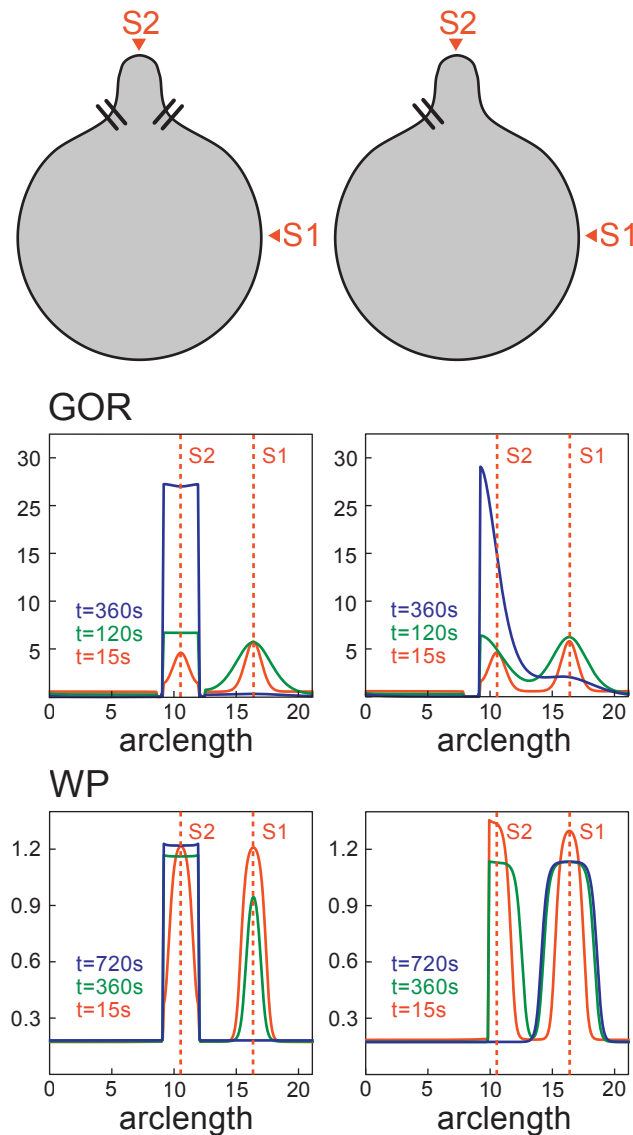


FIGURE 5. The influence of diffusion barriers on the membrane are investigated for the GOR and WP model according to results section (C). In contrast to section (C), the positions of the stimuli S_1 and S_2 are switched to demonstrate the strong effect of the barriers. Hence, the weaker stimulus is located at the protrusion. A two-sided diffusion barrier is placed around the signal location S_1 [right column]. An impermeable area with no diffusion is placed at the left-hand side next to the signal location S_1 [left column].

molecules are accumulated on the membrane, the gradient is especially large in between S_1 and the boundary of the obstacle. The weaker stimulus S_2 eventually dominates the process for both the WP and the GOR model because of better supply with cytosolic molecules. Steady state is reached even earlier as in the case without internal obstacle which means that the organelle actually accelerates the polarization process.

Since there are many organelles of different sizes and shapes in the cell, we also investigate which influence the size of the organelles have. For this, we replace the large oval organelle by two and three smaller circular organelles, see Figure 6 center columns. The smaller organelles were placed at approximately the same distance to S_1 as the larger organelle of the first experiment. Interestingly, the two examined models exhibit different sensitivities to the changed setup.

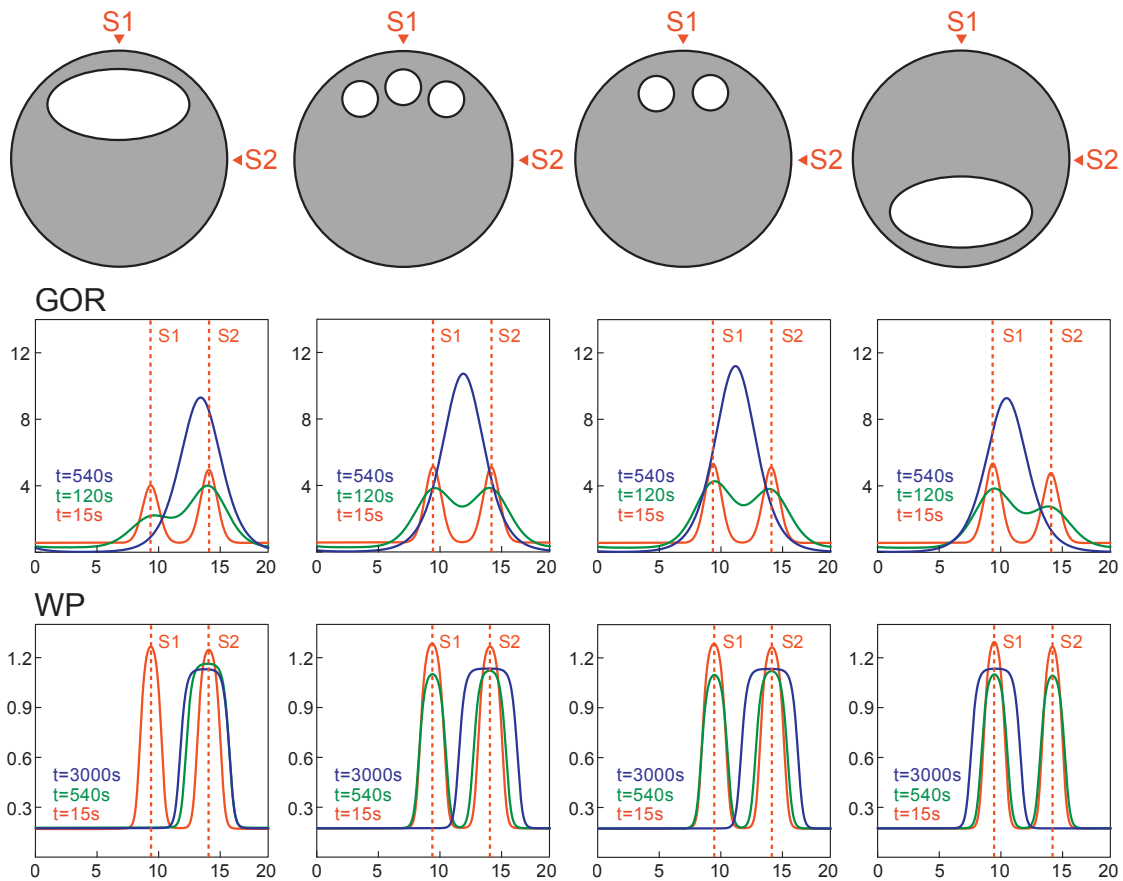


FIGURE 6. The influence of cytosolic diffusion barriers with the GOR and the WP models is investigated, see results section (D). “Organelles” (represented by circles or ellipses) which serve as diffusion barriers are placed at different positions. Two stimuli S_1 and S_2 of different strengths are applied. Stimulus S_1 at the top prevails only if the organelle is sufficiently far away (center or bottom positions). With the organelles placed close to the stronger stimulus S_1 , it is suppressed and S_2 dominates.

For the GOR model the effect of the large organelle is very clear and the cell polarizes at S_2 . For two and three small organelles the cluster gradually moves closer towards the location of the stronger stimulus S_1 . It can also be seen that for the large organelle the cytosolic volume is smaller than for two and three obstacles and since we started the simulations with the same initial concentration there are also less molecules in the cytosol. Therefore, the steady state cluster is slightly smaller than for three and two small organelles.

For the WP model, we observe a significant change of outcomes with two or three obstacles when compared to the first single obstacle setup. The polarization time increases with three obstacles which is even more pronounced in the setting with two obstacles. For instance, the polarization is almost completed after $500s$ while it takes roughly $1000s$ for two and three organelles and even $3000s$ in the case that the organelle is placed at the bottom and therefore has only little impact on the polarization. Nevertheless, the same steady state is reached in all three setups.

We conclude that the GOR model is more gradually influenced by the form of the organelles in the cytosol, while the steady state of the WP model behaves rather switch-like with respect to the introduction of different cytosolic diffusion barriers.

DISCUSSION

Cell polarization is a fundamental process during cell division, cell differentiation and directed growth. In this paper we focus on the crucial initial phase of polarization when a polarization site is established. Since spatial aspects are often neglected in computational as well as experimental investigations, our main question is if and how spatial parameters like cell size, cell shape and spatial inhomogeneities influence the polarization process.

Our study is based on a conceptual two component model which describes the shuttling of one molecule from the cytosol to the membrane and vice versa. Various models of this type can be found in the literature. Since many of these models have been formulated and simulated only in a 1D environment, we suggest a consistent expansion of this class of models to 2D and 3D. In the presented framework, different cell shapes, curved membranes, diffusion inhomogeneities and barriers are integrated. This allows us to go beyond the variation of kinetic parameters to the adjustment of several crucial spatial properties. For this, it is essential to perform simulations at least in 2D so that differences of the surface area, of the inner membrane and the volume of the cytosol, but also of cell shape and organelles placed in the cytosol can be represented and taken into account appropriately.

In our study we have shown that the influence of cellular inhomogeneities can be quite dramatic and should certainly be considered when modeling and simulating spatial intracellular processes. For the realizations of the kinetics, we have chosen the GOR model with Turing-type mechanism on the one hand, and a Wave-Pinning WP mechanism on the other hand. With these two realizations we perform a vast number of computational experiments to examine the influence of (A) the cell shape, (B) the cell size, (C) inhomogeneities on the membrane and (D) organelles in the cytoplasm. For the first setup (A) we show that protrusions act as a negative feedback while intrusions act as a positive feedback. This suggests that growth and maintenance of long protrusions or flagella is complicated for a cell due to limited intracellular transport. Furthermore, we demonstrate that with fixed kinetic parameters there exists an optimal cell size for the GOR and the WP models. For both mechanisms the polarization measured by the average polarization (POL) decreases for larger cells. Moreover, polarization times increase dramatically for large cells. Opposite to that, small cells are unable to polarize at all for the WP and GOR mechanism. An optimum for the suggested parameters and both models could be found for cells with a diameter between $5\mu m$ and $10\mu m$. Diffusion inhomogeneities on the membrane were investigated in setup (C). We show that diffusion barriers can act as a positive feedback on cluster formation. Diffusion on the membrane usually counteracts cluster formation. Hence, hindering membrane diffusion yields an amplification of the signal. As a consequence, the ability to grow large protrusions is enhanced by diffusion barriers on the membrane. In experimental setup (D), we introduce different organelles into the cytosol. We demonstrate that reduced transport due to obstacles leads to a change of the polarization behaviour despite fast cytosolic diffusion. In particular, placing an organelle in the vicinity of a cluster limits the membrane-cytosolic shuttling and therefore also limits the possible growth of the cluster.

The results of this paper are based on static geometries and are therefore important to consider for cells that move or grow slowly in comparison to the diffusion and polarization processes. These assumptions are valid for many fungi, but also plant cells or neurons. Apart from this, the observation that spatial inhomogeneities may significantly influence intracellular transport processes is generically applicable to most cells and demands for further research.

In this work we assume relatively small cells with a diameter of approximately $6\mu m$ and vary the cell size between $1.5\mu m$ to $15\mu m$. However, spatial effects on transport processes become more severe for larger and geometrically more complex cells. Neurons for instance grow large dendrites that detect various stimuli. It has been shown in earlier work that Turing patterns and phosphorylation systems can occur especially in larger cells [7] considering biochemical networks in space. Here, different cell sizes

have been considered, but not the important conceptual effects of cell shape and inhomogeneities on the membrane and in the cytosol.

Recent advances in imaging techniques such as total internal reflection fluorescence (TIRF) and confocal and electron microscopy have the potential to provide quantitative data for effects of cell shape and spatial inhomogeneities. Computer tomographic images of cells can be translated into computational meshes and could serve as a basis for spatial modeling and simulation in the future.

Our results already suggest many spatial effects that could be investigated with such methods. Therefore, we hope that our approach leads to experimental investigations that give more insight into fundamental processes such as cell differentiation, directed growth and cell division.

METHODS

Polarization measures. For a comparison of the models we employ different polarization measures [9, 27] which provide an indication about the localization and strength of a polarization. The first measure is related to the largest value of the surface concentration which is denoted by $u_f = \max_{\vec{x} \in M^{\text{cell}}} u(\vec{x})$. For the comparison of varying concentrations we define the average polarization by

$$(10) \quad \text{POL}(u) = \frac{1}{|M^{\text{cell}}|} \cdot \frac{u_f - \bar{u}}{\bar{u}},$$

$$\bar{u} = \frac{1}{|M^{\text{cell}}|} \int_{M^{\text{cell}}} u \, dA.$$

This measure gives us information on direction and magnitude of polarization. However, the size of the cluster and its relative mass is not reflected. To account for this information, we employ a second measure called the "polarization factor" defined by

$$(11) \quad \text{PF}(u) = 1 - 2 \frac{M_{\text{pol}}(u)}{|M^{\text{cell}}|},$$

$$M_{\text{pol}}(u) = \min \left\{ |B_R(x_f) \cap M^{\text{cell}}| \text{ such that } \int_{B_R(x_f) \cap M^{\text{cell}}} u \, dA = \frac{1}{2} \int_{M^{\text{cell}}} u \, dA \right\},$$

where $\vec{x}_f \in M^{\text{cell}}$ such that $u_f = u(\vec{x}_f)$.

Numerical methods. Simulations were performed using the Distributed and Unified Numerics Environment (DUNE) [4, 3]. We use a finite element method (FEM) of first order based on triangular meshes. The equation for the membrane-bound species is solved on the boundary of the mesh, while the equation for the cytosolic species is solved in the whole meshed domain. The used finite element meshes were generated with Gmsh [20]. All of these meshes comprise several thousand elements to guarantee a high precision of the method (see Figure S4 in the Supporting Text). More detailed information on the utilized numerical methods and example meshes can be found in the supplement.

In the following appendix, we give more details concerning the models and the numerical methods that are used to solve the model equation systems of the main text with the finite element method. Furthermore, additional illustrations are depicted and explained in Figures S1 to S5. An overview of units and values of important quantities is provided in Table S1.

APPENDIX A. MATHEMATICAL MODELS

A.1. 1D modeling framework. One way to understand basic mechanisms of cell polarity is the investigation of partial differential equations where the geometry of the cell is reduced to one space dimension. With reduced models of this kind basic features of the reaction-diffusion dynamics can be captured. The cell is represented by an interval $[0, L]$ which can be either interpreted as a cell diameter transect [23] or the circumference [34] of the cell. In the first case the ends of the interval represent front and back of the cell, in the latter case the ends of the interval are glued together and periodic boundary conditions have to be employed. Here, we only introduce the first interpretation. The set of partial differential equations (PDEs) reads

$$(12) \quad \frac{\partial u}{\partial t} = D_u \frac{\partial^2 u}{\partial x^2} + f(u, v), \quad x \in [0, L], t \in [0, T], L \in \mathbb{R}, T \in \mathbb{R}^+$$

$$(13) \quad \frac{\partial v}{\partial t} = D_v \frac{\partial^2 v}{\partial x^2} - f(u, v),$$

with some initial values $u(\cdot, 0)$ and $v(\cdot, 0)$ in $[0, L]$ and no-flux boundary conditions

$$(14) \quad \frac{\partial u}{\partial x}(0, t) = \frac{\partial u}{\partial x}(L, t) = \frac{\partial v}{\partial x}(0, t) = \frac{\partial v}{\partial x}(L, t) = 0.$$

A.2. 2D and 3D modeling framework. While the 1D modeling framework neglects details of the cell geometry, models in 2D or 3D can also account for the spatial structure of a cell. In our models the computational domain comprises the cytosolic volume $V^{\text{cyt}} \subset \mathbb{R}^d$, $d \in \{2, 3\}$, the outer cell membrane $M^{\text{cell}} \subset \partial V^{\text{cyt}}$ and membranes $M^{\text{org}} = \partial V^{\text{cyt}} \setminus M^{\text{cell}}$ that separate the organelles from the cytosol. A sketch of the computational domain can be seen in Figure S1. Furthermore, we equip our models with diffusion rates which are not necessarily constant along the cell compartments M^{cell} and V^{cyt} . Given some initial values $u(\cdot, 0)$ on M^{cell} and $u(\cdot, 0)$ in V^{cyt} , the model equations incorporating the described cell geometry and inhomogeneous diffusion read

$$(15) \quad \frac{\partial u}{\partial t} = \nabla_{\Gamma} \cdot (D_u \nabla_{\Gamma} u) + f(u, v|_{M^{\text{cell}}}) \quad \text{on } M^{\text{cell}} \times [0, T],$$

$$(16) \quad \frac{\partial v}{\partial t} = \nabla \cdot (D_v \nabla v) \quad \text{in } V^{\text{cyt}} \times [0, T],$$

with boundary conditions

$$(17) \quad -D_v \nabla v \cdot \vec{n} = f(u, v|_{M^{\text{cell}}}) \quad \text{on } M^{\text{cell}} \times [0, T],$$

$$(18) \quad -D_v \nabla v \cdot \vec{n} = 0 \quad \text{on } M^{\text{org}} \times [0, T]$$

for the cytosolic equation (16), where \vec{n} denotes the vector field of outer unit normals on M^{cell} and M^{org} , respectively. For this system of equations we have mass conservation

$$(19) \quad \underbrace{\int_{M^{\text{cell}}} u \, dA}_{\text{molecules on the membrane}} + \underbrace{\int_{V^{\text{cyt}}} v \, dV}_{\text{molecules in the cytosol}} = K \quad \text{for each } t \in [0, T],$$

where $K \in \mathbb{R}$. This conservation property directly follows from the model equations' weak formulation, see Section B.1.

A.3. The wave-pinning model. The wave-pinning (WP) model is based on the membrane-cytosol cycling of Rho proteins [37]. It is focused on the case of a single active-inactive pair. The active, membrane-bound form is represented by its concentration u , whereas the inactive form is represented

by its concentration v . The interplay of activation and binding to the membrane via GEFs and its dissociation via GAPs is described by a kinetic function

$$(20) \quad f_{\text{WP}}(u, v) = \left(k_0 + \frac{\gamma u^2}{K^2 + u^2} \right) v - \delta u.$$

The original model in [37] was formulated and simulated in the 1D modeling framework introduced in Section A.1, where $f(u, v) := f_{\text{WP}}(u, v)$. Using the same kinetic function in the modeling framework from Section A.2, we get a formulation of the model in 2D or 3D. In Figure S3 we compare the results of a simulation which is performed using both modeling frameworks. For the 2D modeling framework from Section A.2 a circular cell with a diameter of $6\mu\text{m}$ was used. The domain for the 1D simulation is an interval with a length corresponding to the circumference of the circular cell. The model behaviour of 1D simulation and 2D simulation in the initial phase is essentially the same. Both simulations result in one cluster of the same amplitude. However, due to a different geometry and surface/volume ratio the size and position of the cluster differs. The results are very similar, indicating that our implementation for higher dimension discretizations is correct.

A.4. The Goryachev model. The Goryachev (GOR) model [21] describes the initial phase of polarization of budding yeast. In this model the spatiotemporal dynamics of a Cdc42 cluster during the budding process of *S. cerevisiae* is modeled, by describing the cycling process from membrane to cytosol. The fast diffusing cytosolic species with its concentration v represents the GDP-bound inactive Cdc42 complex. The active, membrane-bound form of Cdc42 is represented by the surface concentration u . The GOR model was originally formulated in 3D and simulated using Virtual Cell [12]. Instead of the detailed biochemical model we use a condensed model that captures the basic properties and was also proposed in [21]. This basic model employs the kinetics

$$(21) \quad f_{\text{GOR}}(u, v) = \alpha E_c u^2 v + \beta E_c u v - \gamma u,$$

$$E_c = \frac{E_c^0}{1 + \int_{M^{\text{cell}}} g(u) dA}.$$

Here, the parameters α , β and γ are constants and E_c represents the Cdc24-Bem1 complex. For simplicity we assume E_c to be constant. We formulate the GOR model in the 1D modeling framework from Section A.1 and in the 2D and 3D modeling framework from Section A.2, both using $f(u, v) := f_{\text{GOR}}(u, v)$. For a simulation performed in 1D and in 2D a comparison of the results is shown in Figure S3. Again we used a circular cell with a diameter of $6\mu\text{m}$ for the 2D simulation and an interval with a length corresponding to the circumference of the circular cell for the 1D simulation. The model behaviour of 1D simulation and 2D simulation in the initial phase is essentially the same and both simulations result in one cluster. While the qualitative behaviour is essentially the same for this cell geometry, the size of the cluster differs in the 1D and 2D simulation due to a different surface/volume ratio.

APPENDIX B. NUMERICAL METHODS USED FOR SIMULATIONS

In the following, the numerical approach is described that is used for simulating the mathematical models formulated in the 2D and 3D modeling framework from Section A.2. As for all numerical approaches, the fundamental idea is to discretize the mathematical model. This process yields a system of algebraic equations which can be solved using a computer.

To separate discretization in space and time, we use the well-known method of lines, see e.g. [46], and start with a semidiscretization in space using finite element methods of first order based on triangular meshes. Given a triangular mesh which describes the geometrical setup introduced in Section A, the equation for the volume species is treated by the standard conforming finite element approach,

employing Lagrange basis functions of polynomial degree one. To treat the equation describing the membrane-bound species, we apply a surface finite element method on the boundary of the mesh using a restriction of the same volumetric basis functions. This enables implementing the numerical approach with tools provided by standard software frameworks for scientific computing. The idea of performing spatial discretization by combining the conforming finite element method and surface finite elements on the same mesh is related to the procedure presented in [16], where a similar approach is used for the discretization of a coupled elliptic model problem.

With the method of lines, different schemes can be employed for the discretization in time. In accordance with our spatial discretization we restrict ourselves to first-order schemes. We use both a fully implicit scheme and a semi-implicit scheme inspired by the implicit-explicit (IMEX) Euler method presented e.g. in [26]. The idea of the IMEX method is to treat the spatially discretized reaction part of the system explicitly. Therefore, on the one hand the membrane equation and the cytosolic equation are decoupled and thus can be treated separately, and on the other hand the non-linearities are treated explicitly which enables using a linear solver. On the downside, an explicit treatment of the reaction part can affect the stability of the scheme in the reaction-dominated case and for a stiff reaction part in general [26]. Our semi-implicit scheme decouples membrane and cytosolic equations while still treating the reaction part of each separate equation and its non-linearities implicitly. For each equation this is done by treating only the unknowns of the other equation explicitly.

B.1. Weak formulation. First, we derive a weak formulation of model equations (15) – (18) in order to apply finite element methods for semidiscretization in space. Let $\mathcal{V}^{\text{vol}} := H^1(V^{\text{cyt}})$ denote the usual Sobolev space containing weak solutions of elliptic equations in the bulk domain V^{cyt} . A natural counterpart containing weak solutions of elliptic equations on hypersurfaces are surface Sobolev spaces [55, 13, 14]. To treat equation (15) on the closed hypersurface M^{cell} we therefore define the surface Sobolev space $\mathcal{V}^{\text{sur}} := H^1(M^{\text{cell}})$.

Multiplication of model equations (15) and (16) with some test functions $\varphi_u \in H^1(M^{\text{cell}})$ respectively $\varphi_v \in H^1(V^{\text{cyt}})$ results in

$$(22) \quad \frac{d}{dt} \int_{M^{\text{cell}}} u \varphi_u \, dA = \int_{M^{\text{cell}}} \nabla_{\Gamma} \cdot (D_u(x) \nabla_{\Gamma} u) \varphi_u \, dA + \int_{M^{\text{cell}}} f(u, v|_{M^{\text{cell}}}) \varphi_u \, dA,$$

$$(23) \quad \frac{d}{dt} \int_{V^{\text{cyt}}} v \varphi_v \, dV = \int_{V^{\text{cyt}}} \nabla \cdot (D_v(x) \nabla v) \varphi_v \, dV.$$

Application of the integration by parts formula for Sobolev spaces in (23), and its analog derivable from the surface divergence theorem (see [14] and references therein) in (22), yields

$$(24) \quad \frac{d}{dt} \int_{M^{\text{cell}}} u \varphi_u \, dA = - \int_{M^{\text{cell}}} D_u(x) \nabla_{\Gamma} u \cdot \nabla_{\Gamma} \varphi_u \, dA + \int_{M^{\text{cell}}} f(u, v|_{M^{\text{cell}}}) \varphi_u \, dA,$$

$$(25) \quad \frac{d}{dt} \int_{V^{\text{cyt}}} v \varphi_v \, dV = - \int_{V^{\text{cyt}}} D_v(x) \nabla v \cdot \nabla \varphi_v \, dV + \int_{\partial V^{\text{cyt}}} D_v(x) \frac{\partial v}{\partial \vec{n}} \varphi_v|_{\partial V^{\text{cyt}}} \, dA.$$

Due to the boundary conditions (17) and (18), together with ∂V^{cyt} being the disjoint union $M^{\text{cell}} \cup M^{\text{org}}$, this is equivalent to

$$(26) \quad \frac{d}{dt} \int_{M^{\text{cell}}} u \varphi_u \, dA = - \int_{M^{\text{cell}}} D_u(x) \nabla_{\Gamma} u \cdot \nabla_{\Gamma} \varphi_u \, dA + \int_{M^{\text{cell}}} f(u, v|_{M^{\text{cell}}}) \varphi_u \, dA,$$

$$(27) \quad \frac{d}{dt} \int_{V^{\text{cyt}}} v \varphi_v \, dV = - \int_{V^{\text{cyt}}} D_v(x) \nabla v \cdot \nabla \varphi_v \, dV - \int_{M^{\text{cell}}} f(u, v|_{M^{\text{cell}}}) \varphi_v|_{M^{\text{cell}}} \, dA.$$

The weak formulation of model equations (15) – (18) now is to look for a solution $(u, v) \in L^2([0, T], \mathcal{V}^{\text{sur}}) \times L^2([0, T], \mathcal{V}^{\text{vol}})$, such that for each $t \in [0, T]$

$$(28) \quad \frac{d}{dt} \int_{M^{\text{cell}}} u \varphi_u \, dA = - \int_{M^{\text{cell}}} D_u(x) \nabla_{\Gamma} u \cdot \nabla_{\Gamma} \varphi_u \, dA + \int_{M^{\text{cell}}} f(u, v|_{M^{\text{cell}}}) \varphi_u \, dA \quad \text{for all } \varphi_u \in \mathcal{V}^{\text{sur}},$$

$$(29) \quad \frac{d}{dt} \int_{V^{\text{cyt}}} v \varphi_v \, dV = - \int_{V^{\text{cyt}}} D_v(x) \nabla v \cdot \nabla \varphi_v \, dV - \int_{M^{\text{cell}}} f(u, v|_{M^{\text{cell}}}) \varphi_v \, dA \quad \text{for all } \varphi_v \in \mathcal{V}^{\text{vol}}.$$

Note that also the constant test functions $\varphi_u \equiv 1$ respectively $\varphi_v \equiv 1$ are permitted which yields mass conservation (19).

B.2. Semidiscretization in space. To obtain a semidiscretized system, we combine the conforming finite element approach (FEM) and a surface finite element method (SFEM). The FEM is a standard approach which is well-known to literature. See e.g. [10, 6] to gain an insight into the methodology. An SFEM developed in [13] can be seen as a natural generalization, as the idea of FEM is transferred to elliptic equations on hypersurfaces. Its extension [14] to treating parabolic equations, like membrane equation (17), provides the basis for the SFEM that we use.

Both approaches are based on an approximation of the bulk domain V^{cyt} and the hypersurface M^{cell} , each by a triangulable geometrical object, and corresponding meshes. For simplicity, we assume V^{cyt} to be a polyhedral domain that can be exactly represented by a triangular mesh \mathcal{T}_h . With M^{cell} being part of the boundary of V^{cyt} , it corresponds to a set of boundary entities of \mathcal{T}_h which make up a surface mesh $\mathcal{T}_h^{\text{sur}} \subset \mathcal{T}_h$. Each method uses its corresponding mesh to set up a finite-dimensional function space usable for spatial discretization of the model equations. In particular, we replace the function spaces \mathcal{V}^{sur} and \mathcal{V}^{vol} by finite-dimensional conforming function spaces $\mathcal{V}_h^{\text{sur}} \subset \mathcal{V}^{\text{sur}}$ respectively $\mathcal{V}_h^{\text{vol}} \subset \mathcal{V}^{\text{vol}}$ and seek a semidiscrete solution $(u_h, v_h) \in L^2([0, T], \mathcal{V}_h^{\text{sur}}) \times L^2([0, T], \mathcal{V}_h^{\text{vol}})$, such that for each $t \in [0, T]$

$$(30) \quad \frac{d}{dt} \int_{M^{\text{cell}}} u_h \varphi_{u,h} \, dA = - \int_{M^{\text{cell}}} D_u(x) \nabla_{\Gamma} u_h \cdot \nabla_{\Gamma} \varphi_{u,h} \, dA + \int_{M^{\text{cell}}} f(u_h, v_h|_{M^{\text{cell}}}) \varphi_{u,h} \, dA \quad \text{for all } \varphi_{u,h} \in \mathcal{V}_h^{\text{sur}},$$

$$(31) \quad \frac{d}{dt} \int_{V^{\text{cyt}}} v_h \varphi_{v,h} \, dV = - \int_{V^{\text{cyt}}} D_v(x) \nabla v_h \cdot \nabla \varphi_{v,h} \, dV - \int_{M^{\text{cell}}} f(u_h, v_h|_{M^{\text{cell}}}) \varphi_{v,h} \, dA \quad \text{for all } \varphi_{v,h} \in \mathcal{V}_h^{\text{vol}}.$$

As discrete function spaces, we employ the node-based Lagrange spaces of polynomial degree one on $\mathcal{T}_h^{\text{sur}}$ and \mathcal{T}_h . With the basis functions $\{\varphi_{u,h}^{x_h}\}_{x_h \in \mathcal{X}_h^{\text{sur}}}$ of $\mathcal{V}_h^{\text{sur}}$ and the basis functions $\{\varphi_{v,h}^{x_h}\}_{x_h \in \mathcal{X}_h}$

of $\mathcal{V}_h^{\text{vol}}$, where $\mathcal{X}_h^{\text{sur}}$ and \mathcal{X}_h are the sets of nodes associated with the basis functions, we deduce

$$(32) \quad \frac{d}{dt} \int_{M^{\text{cell}}} u_h \varphi_{u,h}^{x_h} dA = - \int_{M^{\text{cell}}} D_u(x) \nabla_{\Gamma} u_h \cdot \nabla_{\Gamma} \varphi_{u,h}^{x_h} dA + \int_{M^{\text{cell}}} f(u_h, v_h|_{M^{\text{cell}}}) \varphi_{u,h}^{x_h} dA \quad \text{for all } x_h \in \mathcal{X}_h^{\text{sur}},$$

$$(33) \quad \frac{d}{dt} \int_{V^{\text{cvt}}} v_h \varphi_{v,h}^{x_h} dV = - \int_{V^{\text{cvt}}} D_v(x) \nabla v_h \cdot \nabla \varphi_{v,h}^{x_h} dV - \int_{M^{\text{cell}}} f(u_h, v_h|_{M^{\text{cell}}}) \varphi_{v,h}^{x_h} dA \quad \text{for all } x_h \in \mathcal{X}_h.$$

The semidiscrete solution (u_h, v_h) can be represented as

$$(34) \quad u_h = \sum_{\tilde{x}_h \in \mathcal{X}_h^{\text{sur}}} b_u^{\tilde{x}_h}(t) \varphi_{u,h}^{\tilde{x}_h} \quad \text{and} \quad v_h = \sum_{\tilde{x}_h \in \mathcal{X}_h} b_v^{\tilde{x}_h}(t) \varphi_{v,h}^{\tilde{x}_h}$$

by time-dependent coefficient vectors $\vec{b}_u(t) = (b_u^{\tilde{x}_h}(t))_{\tilde{x}_h \in \mathcal{X}_h^{\text{sur}}}$ and $\vec{b}_v(t) = (b_v^{\tilde{x}_h}(t))_{\tilde{x}_h \in \mathcal{X}_h}$. Therefore, we get a system of ordinary differential equations

$$(35) \quad \left. \begin{aligned} \mathcal{M}_u \cdot \vec{b}'_u(t) + \mathcal{S}_u \cdot \vec{b}_u(t) &= \vec{f}_u(\vec{b}_u(t), \vec{b}_v(t)) \\ \mathcal{M}_v \cdot \vec{b}'_v(t) + \mathcal{S}_v \cdot \vec{b}_v(t) &= -\vec{f}_v(\vec{b}_u(t), \vec{b}_v(t)) \end{aligned} \right\} \quad \text{on } [0, T],$$

with mass and stiffness matrices

$$(36) \quad \mathcal{M}_u := \left(\int_{M^{\text{cell}}} \varphi_{u,h}^{\tilde{x}_h} \varphi_{u,h}^{x_h} dA \right)_{x_h \in \mathcal{X}_h^{\text{sur}}, \tilde{x}_h \in \mathcal{X}_h^{\text{sur}}}, \quad \mathcal{S}_u := \left(\int_{M^{\text{cell}}} D_u(x) \nabla_{\Gamma} \varphi_{u,h}^{\tilde{x}_h} \cdot \nabla_{\Gamma} \varphi_{u,h}^{x_h} dA \right)_{x_h \in \mathcal{X}_h^{\text{sur}}, \tilde{x}_h \in \mathcal{X}_h^{\text{sur}}},$$

$$(37) \quad \mathcal{M}_v := \left(\int_{V^{\text{cvt}}} \varphi_{v,h}^{\tilde{x}_h} \varphi_{v,h}^{x_h} dA \right)_{x_h \in \mathcal{X}_h, \tilde{x}_h \in \mathcal{X}_h}, \quad \mathcal{S}_v := \left(\int_{V^{\text{cvt}}} D_v(x) \nabla \varphi_{v,h}^{\tilde{x}_h} \cdot \nabla \varphi_{v,h}^{x_h} dA \right)_{x_h \in \mathcal{X}_h, \tilde{x}_h \in \mathcal{X}_h},$$

and vector valued right hand side functions \vec{f}_u, \vec{f}_v ,

$$(38) \quad \vec{f}_u(\vec{b}_u(t), \vec{b}_v(t)) := \left(\int_{M^{\text{cell}}} f \left(\sum_{\tilde{x}_h \in \mathcal{X}_h^{\text{sur}}} b_u^{\tilde{x}_h}(t) \varphi_{u,h}^{\tilde{x}_h}, \sum_{\tilde{x}_h \in \mathcal{X}_h} b_v^{\tilde{x}_h}(t) \varphi_{v,h}^{\tilde{x}_h} |_{M^{\text{cell}}} \right) \varphi_{u,h}^{x_h} dA \right)_{x_h \in \mathcal{X}_h^{\text{sur}}},$$

$$(39) \quad \vec{f}_v(\vec{b}_u(t), \vec{b}_v(t)) := \left(\int_{M^{\text{cell}}} f \left(\sum_{\tilde{x}_h \in \mathcal{X}_h^{\text{sur}}} b_u^{\tilde{x}_h}(t) \varphi_{u,h}^{\tilde{x}_h}, \sum_{\tilde{x}_h \in \mathcal{X}_h} b_v^{\tilde{x}_h}(t) \varphi_{v,h}^{\tilde{x}_h} |_{M^{\text{cell}}} \right) \varphi_{v,h}^{x_h} dA \right)_{x_h \in \mathcal{X}_h}.$$

B.2.1. SFEM matrix/vector assembly via volumetric FEM basis functions. As we use node-based Lagrange spaces of the same polynomial degree based on the same triangular mesh, the set of Lagrange nodes of $\mathcal{V}_h^{\text{sur}}$ can be described as $\mathcal{X}_h^{\text{sur}} = \{x_h \in \mathcal{X}_h \mid x_h \in M^{\text{cell}}\} \subset \mathcal{X}_h$. Moreover, the employed Lagrange basis functions have the property, that

$$(40) \quad \varphi_{u,h}^{x_h} = \varphi_{v,h}^{x_h} |_{M^{\text{cell}}} \quad \forall x_h \in \mathcal{X}_h^{\text{sur}}.$$

Thus, instead of directly implementing the SFEM ansatz space $\mathcal{V}_h^{\text{sur}}$, the constrained function space

$$(41) \quad \partial \mathcal{V}_h^{\text{vol}} := \{v \in \mathcal{V}_h^{\text{vol}} \mid v(x_h) = 0 \text{ for } x_h \in \mathcal{X}_h \setminus \mathcal{X}_h^{\text{sur}}\} \subset \mathcal{V}_h^{\text{vol}}$$

can be utilized to perform the assembly of $\mathcal{M}_u, \mathcal{S}_u, \vec{f}_u$ and \vec{f}_v . In particular, the restriction of its basis $\{\varphi_{v,h}^{x_h}\}_{x_h \in \mathcal{X}_h^{\text{sur}}}$ to the set M^{cell} equals the Lagrange basis $\{\varphi_{u,h}^{x_h}\}_{x_h \in \mathcal{X}_h^{\text{sur}}}$ of $\mathcal{V}_h^{\text{sur}}$.

Note that $\partial \mathcal{V}_h^{\text{vol}} \not\subset \mathcal{V}_h^{\text{sur}}$. Hence, the surface component of the numerical solution can not be directly represented in the space $\partial \mathcal{V}_h^{\text{vol}}$. Nevertheless, using the identity $\partial \mathcal{V}_h^{\text{vol}} |_{M^{\text{cell}}} = \mathcal{V}_h^{\text{sur}}$, the semidiscrete solution $(u_h, v_h) \in L^2([0, T], \mathcal{V}_h^{\text{sur}}) \times L^2([0, T], \mathcal{V}_h^{\text{vol}})$ can be calculated as

$$(42) \quad u_h = \sum_{\tilde{x}_h \in \mathcal{X}_h^{\text{sur}}} b_u^{\tilde{x}_h}(t) \varphi_{v,h}^{\tilde{x}_h} |_{M^{\text{cell}}} \quad \text{and} \quad v_h = \sum_{\tilde{x}_h \in \mathcal{X}_h} b_v^{\tilde{x}_h}(t) \varphi_{v,h}^{\tilde{x}_h}.$$

B.3. Fully discretized systems. System (35) can be equivalently written as

$$(43) \quad \vec{b}'_u(t) = -\mathcal{M}_u^{-1} \mathcal{S}_u \cdot \vec{b}_u(t) + \mathcal{M}_u^{-1} \cdot \vec{f}_u(\vec{b}_u(t), \vec{b}_v(t)),$$

$$(44) \quad \vec{b}'_v(t) = -\mathcal{M}_v^{-1} \mathcal{S}_v \cdot \vec{b}_v(t) - \mathcal{M}_v^{-1} \cdot \vec{f}_v(\vec{b}_u(t), \vec{b}_v(t)),$$

or as

$$(45) \quad \vec{b}'(t) = -\mathcal{M}^{-1} \mathcal{S} \cdot \vec{b}(t) + \mathcal{M}^{-1} \cdot \vec{f}(\vec{b}(t)) \quad \text{on } [0, T],$$

using the notation

$$(46) \quad \mathcal{M} := \begin{pmatrix} \mathcal{M}_u & 0 \\ 0 & \mathcal{M}_v \end{pmatrix}, \quad \mathcal{S} := \begin{pmatrix} \mathcal{S}_u & 0 \\ 0 & \mathcal{S}_v \end{pmatrix}, \quad \vec{b}(t) := \begin{pmatrix} \vec{b}_u(t) \\ \vec{b}_v(t) \end{pmatrix} \quad \text{and} \quad \vec{f}(\vec{b}(t)) := \begin{pmatrix} \vec{f}_u(\vec{b}(t)) \\ \vec{f}_v(\vec{b}(t)) \end{pmatrix}.$$

For discretization in time the interval $[0, T]$ is split into sub-intervals $[t_k, t_{k-1}]$ of length $\tau_k := t_k - t_{k-1}$, $k = 1 \dots, K$, with $0 = t_0 < t_1 < \dots < t_k < \dots < t_{K-1} < t_K = T$. By \vec{b}^k we denote a time-dependent coefficient vector \vec{b} evaluated at t_k . Employing the backward Euler method in (45), we end up with a system of nonlinear algebraic equations

$$(47) \quad \vec{b}^k = \vec{b}^{k-1} - \tau \mathcal{M}^{-1} \mathcal{S} \cdot \vec{b}^k + \tau \mathcal{M}^{-1} \cdot \vec{f}(\vec{b}^k), \quad k \in \{1, \dots, K\},$$

which can be solved e.g. using a multidimensional Newton's method. However, solving this fully discretized system can get very time-consuming, especially when a fine finite element mesh is used, as this results in high-dimensional coefficient vectors. For this reason, we employ a semi-implicit scheme for temporal discretization which decouples equations (43) and (44). In particular, we use the backward Euler method separately for each equation, while treating the unknowns of the other equation explicitly. In contrast to the IMEX Euler method (see e.g. [26]) the unknowns of each separate equation are thus treated fully implicit. The fully discretized system then reads

$$(48) \quad \left. \begin{aligned} \vec{b}_u^k &= \vec{b}_u^{k-1} - \tau \mathcal{M}_u^{-1} \mathcal{S}_u \cdot \vec{b}_u^k + \tau \mathcal{M}_u^{-1} \cdot \vec{f}_u(\vec{b}_u^k, \vec{b}_v^{k-1}) \\ \vec{b}_v^k &= \vec{b}_v^{k-1} - \tau \mathcal{M}_v^{-1} \mathcal{S}_v \cdot \vec{b}_v^k + \tau \mathcal{M}_v^{-1} \cdot \vec{f}_v(\vec{b}_u^{k-1}, \vec{b}_v^k) \end{aligned} \right\} \quad k \in \{1, \dots, K\}$$

and can be solved e.g. using a multidimensional Newton's method for both equations in parallel.

Our experiments have shown no obvious qualitative differences between the solutions computed with both schemes (47) and (48).

B.4. Simulation framework. The presented numerical approach can be implemented with tools provided by standard PDE software frameworks. For the assembly of the required matrices, the framework has to provide the space of simplicial Lagrange finite elements of order one on a triangular mesh. Furthermore, it either has to provide the space of simplicial Lagrange finite elements of order one on the boundary of the same mesh or a mechanism for constraining the degrees of freedom of the volumetric Lagrange space which do not lie on the boundary of the mesh. The latter mechanism usually is available in those frameworks, since constrained degrees of freedom are frequently used to implement Dirichlet boundary conditions.

All of our simulations were performed using the Distributed and Unified Numerics Environment (DUNE) [4, 3]. The numerical discretization schemes were implemented using the discretization module DUNE-PDELab which is based on DUNE. It provides the volumetric finite element space $\mathcal{V}_h^{\text{vol}}$ which in addition can be constrained for SFEM matrix/vector assembly using the space $\partial \mathcal{V}_h^{\text{vol}}$. Furthermore, it features an easy to use assembly infrastructure, as well as the linear solver, nonlinear solver and time-stepping schemes that were used.

The finite element meshes were generated with Gmsh [20], examples of which are depicted in Figure S4. All of these meshes comprise several thousand elements to guarantee a high precision of the

method. Additionally, meshes are refined near the outer cell membrane M^{cell} in our simulations to enable an accurate computation of the coupling process on the surface.

All code and meshes used in this work are freely available from the authors on request.

B.5. Alternative approaches. An alternative approach usable for simulating the mathematical models is presented in [18]. It uses an implicit description of the cellular geometry via level set functions and seems to be promising especially in the context of geometrical setups that are more complex than those investigated in this work, like those arising from real microscopy data. Particularly, it might be useful for coping with a cellular geometry that even evolves in time. Furthermore, already for simple geometries it can be advantageous as there is no need for a customized mesh generation. This can ease the simulation workflow. A similar approach can be found in [50], which also has the advantage of using an implicit geometry description, but uses a diffuse-interface representation via a phase-field function.

Another alternative approach is presented in [41] and implemented in the cell modeling and simulation software Virtual Cell [12]. Though employing a cell-centered finite volume scheme on a regular mesh and thus approximating the membrane M^{cell} in a staircase manner, convergence results for static spherical geometries are presented in [41] that render the method well-suited in the considered case.

APPENDIX C. ASYMPTOTIC ANALYSIS

C.1. WP model. In the following, we want to examine analytically the size of the cluster for the WP model. After stimulation on the cell surface (as performed in the simulations in the main text) a traveling wave occurs that is pinned due to mass conservation of the system. For the WP model the cluster grows mainly into the width but only slightly into the height. In addition to the *POL* measure from the main text, which describes the relative height of the cluster, we therefore introduce a new measure for the relative cluster width as follows:

$$(49) \quad POL^w := \frac{|M^+|}{|M^{\text{cell}}|},$$

where M^+ is the excited region of the cell surface. The excited region of the cell surface is defined as the surface area, where the surface concentration u is higher than the average surface concentration \bar{u} :

$$M^+ := \{\vec{x} \in M^{\text{cell}} | u(\vec{x}) > \bar{u}\} \text{ and}$$

$$\bar{u} = \frac{1}{|M^{\text{cell}}|} \int_{M^{\text{cell}}} u \, dA.$$

Therefore, the POL^w measure compares the size of the excited part (called cluster) to the total surface area of the cell. Due to the structure of the reaction kinetics of the WP model the concentration level of active molecules u on the cell surface separates the cell surface into two parts. The excited part $M^+ \subset M^{\text{cell}}$ of the cell surface is at concentration level u_+ and the not excited part $M^- \subset M^{\text{cell}} \setminus M^+$ is at concentration level u_- . At steady state the concentration in the volume is almost equally distributed and takes the value v_c . Due to mass conservation, in steady state it holds

$$|M^+|u_+ + (|M^{\text{cell}}| - |M^+|)u_- + |V^{\text{cell}}|v_c \approx |M^{\text{cell}}|u(0) + |V^{\text{cell}}|v(0).$$

Solving this equation for the excited area of the cell surface $|M^+|$ we get

$$|M^+| \approx \frac{|M^{\text{cell}}|(u(0) - u_-) + |V^{\text{cell}}|(v(0) - v_c)}{u_+ - u_-}.$$

Using this relation, we can easily approximate the POL^w measure:

$$(50) \quad POL^w \approx \frac{1}{u_+ - u_-} \left((u(0) - u_-) + \frac{|V^{cell}|}{|M^{cell}|} (v(0) - v_c) \right).$$

In the case of a circular/spherical cell this becomes

$$(51) \quad POL^w \approx \frac{1}{u_+ - u_-} \left((u(0) - u_-) + \frac{R}{d} (v(0) - v_c) \right),$$

where $d \in \{2, 3\}$ is the dimension of the computational representation of the cell. Therefore, the relative cluster width grows linearly with the cell size. Note that for a 1D model, the ratio $\frac{|V^{cell}|}{|M^{cell}|}$ is constant and the relative cluster width defined in (50) becomes independent of the cell size. A comparison of the simulated and the approximated cluster width in (50) is presented in Figure S5.

C.2. GOR model. In the following, we investigate the behaviour of the GOR model during the initial phase, in order to estimate the influence of the diffusion parameters on the cluster width. The 1D model is locally a good approximation for the behaviour of higher dimensional models (2D or 3D) in a circular or spherical cell near the steady state [38, 43]. Therefore, we perform the analysis of asymptotics for the corresponding 1D model. For the asymptotic analysis of bulk-surface reaction-diffusion systems in higher dimensions, such as models formulated in the modeling framework from Section A.2, we refer to [45, 31]. Since we want to investigate the model behaviour in the steady state, we introduce

$$\vec{w} = \begin{pmatrix} u - u_0 \\ v - v_0 \end{pmatrix},$$

where u_0 and v_0 are the steady states of the equation system (12), (13). The linearized equations of this system at $\vec{w} = 0$ reads as

$$\frac{\partial \vec{w}}{\partial t} = D \Delta \vec{w} + J \vec{w},$$

where

$$D = \begin{pmatrix} D_m & 0 \\ 0 & D_c \end{pmatrix} \text{ and } J = \begin{pmatrix} f_u & f_v \\ -f_u & -f_v \end{pmatrix}.$$

With this, we define the eigenvalue problem

$$\begin{aligned} \Delta \vec{W} + k^2 \vec{W} &= 0 \\ \text{and } \frac{\partial \vec{W}}{\partial t}(0, t) &= 0, \quad \frac{\partial \vec{W}}{\partial t}(L, t) = 0 \end{aligned}$$

where k is the eigenvalue. Let \vec{W}_k be the corresponding eigenfunction for the wavenumber k . In the special case above this is $\vec{W}_k \propto \cos(n\pi x/L)$ and the wavenumber is $k = n\pi/L$. The wavelength ω is proportional to $1/k$ and is calculated by $\omega = 2\pi L/k$. Since the problem is linear, we look for solutions of the form

$$\vec{w}(\vec{x}, t) = \sum_k c_k \exp(\lambda t) \vec{W}_k,$$

where the constants c_k are determined by a Fourier expansion of the initial condition in terms of W_k . λ is the eigenvalue which determines the temporal growth. With this, we get for each k that

$$\begin{aligned} \lambda W_k &= D \Delta W_k + J W_k \\ &= -D k^2 W_k + J W_k. \end{aligned}$$

We require nontrivial solutions for W_k , so the λ are determined by the roots of the characteristic polynomial

$$\begin{aligned}
 0 &= |\lambda I - J + Dk^2| \\
 &= \begin{vmatrix} \lambda - f_u + D_m k^2 & -f_v \\ f_u & \lambda + f_v + D_c k^2 \end{vmatrix} \\
 &= (\lambda - f_u + D_m k^2)(\lambda + f_v + D_c k^2) + f_v f_u \\
 (52) \quad &= \lambda^2 + \lambda \underbrace{((D_c + D_m)k^2 + f_v - f_u)}_{=A(k)} + \underbrace{D_m D_c k^4 - k^2(D_c f_u - D_m f_v)}_{=B(k)}
 \end{aligned}$$

For a temporal growing wave number k we require λ to be positive. Since $A(k)$ is positive, we only get positive roots for λ iff $B(k) \leq 0$. From this we deduce

$$0 \leq k \leq \sqrt{\frac{D_c f_u - D_m f_v}{D_m D_c}} = k_{max}.$$

The polynomial (52) can also be seen as a function of k^2 . Solving for the value of k where λ is maximal yields

$$k^* = \left\{ \frac{1}{D_c - D_m} \left[-(f_u + f_v) + \left(\sqrt{\frac{D_m}{D_c}} + \sqrt{\frac{D_c}{D_m}} \right) \sqrt{f_u f_v} \right] \right\}^{\frac{1}{2}}.$$

This wave number is the fastest growing for a perturbation near the homogeneous steady state. For the GOR model this results in following values:

	D_c	D_m	k^*	k_{max}
GOR	1	0.0025	0.32	1.26
	3.0	0.015	0.16	0.51

Since the wave length of the fastest growing cluster is linearly dependend on $1/k$, we can conclude that the cluster width during the initial phase is larger for the combination of diffusion coefficients $D_c = 3.0\mu m^2/s$ and $D_m = 0.015\mu m^2/s$ than for the combination $D_c = 1.0\mu m^2/s$ and $D_m = 0.0025\mu m^2/s$. However, the exact cluster width at steady state differs for higher dimensions and is calculated numerically in Figure S5.

APPENDIX D. FIGURES

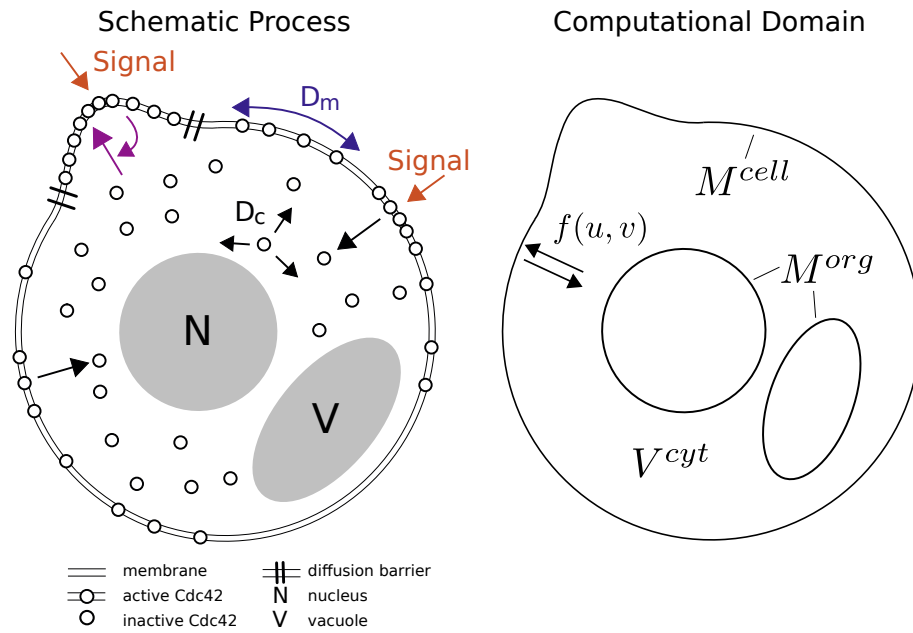
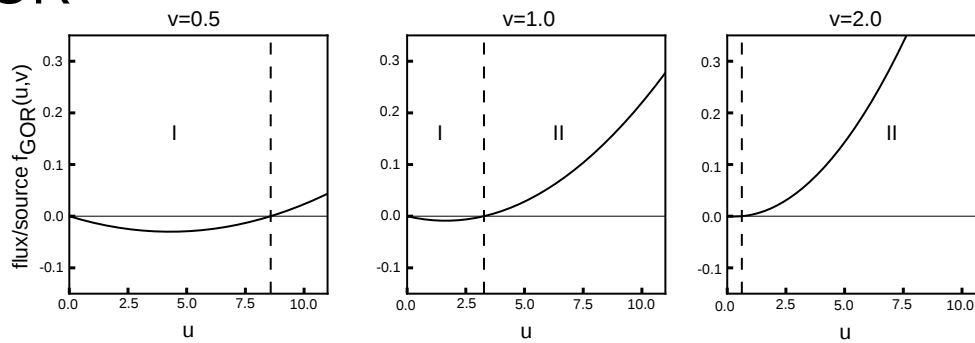


Figure S1 The schematic cell polarization process is shown next to the computational domain. V^{cyt} represents the cytosolic volume, which is an area in 2D and a volume in 3D. M^{cell} and M^{org} are the boundaries of V^{cyt} and describe the outer cell membrane and the organelles' membranes.

GOR



WP

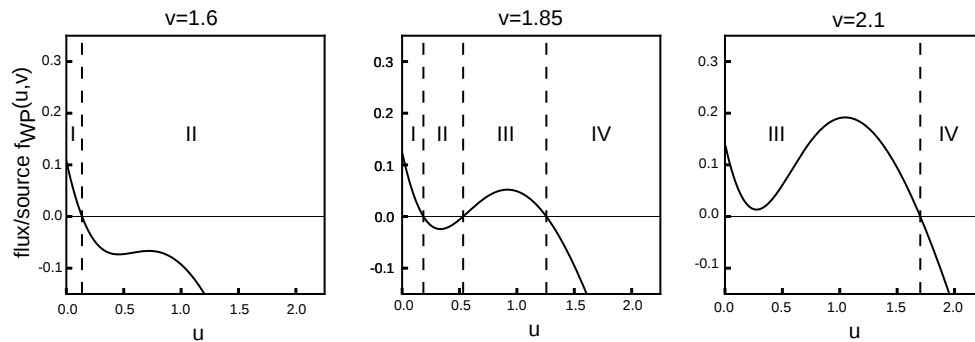


Figure S2 The right hand side of both models, plotted for a fixed volume concentration v .

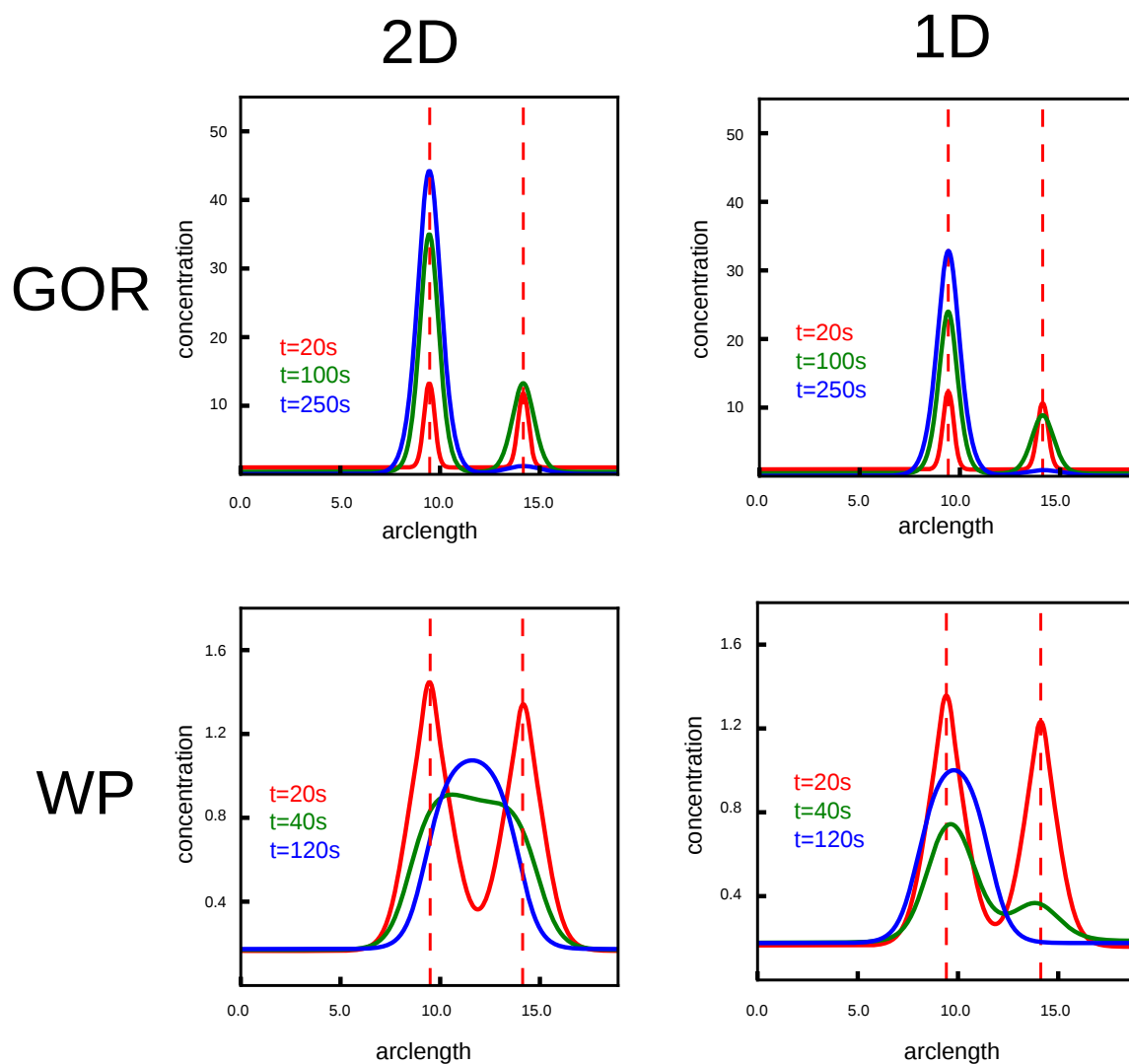


Figure S3 Comparison of a simulation performed in 2D (left) and in 1D (right). The results essentially look the same, especially the steady state profile in the end. Slight differences are expected, since the volume/surface ratio is different in the 1D case and in the 2D case.

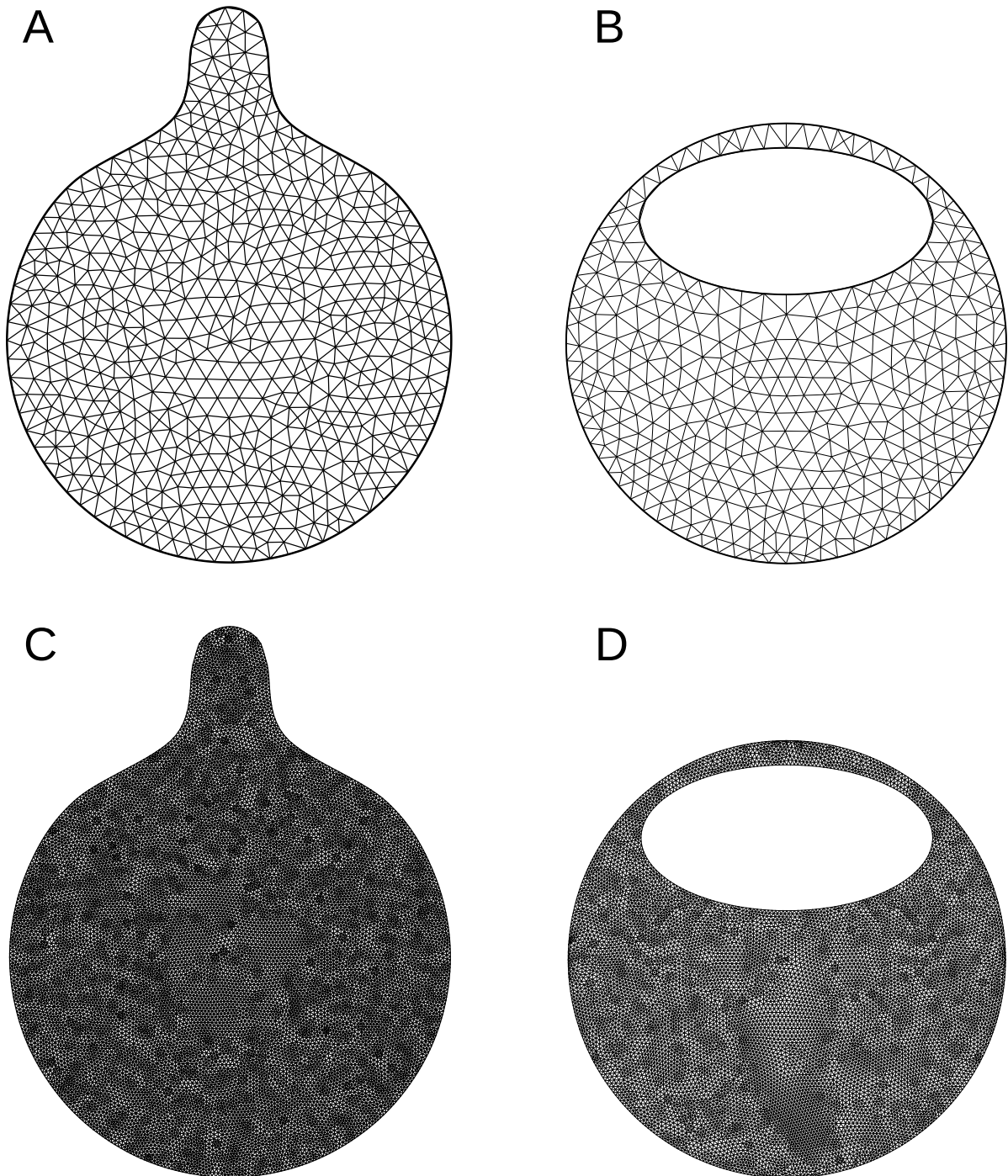


Figure S4 (A+B) Coarse triangular meshes of different cell geometries. The meshes used for the simulations in the main text are refined to guarantee high accuracy of the obtained solution. The mesh in (C) contains 24792 elements and in (D) contains 20632 elements.

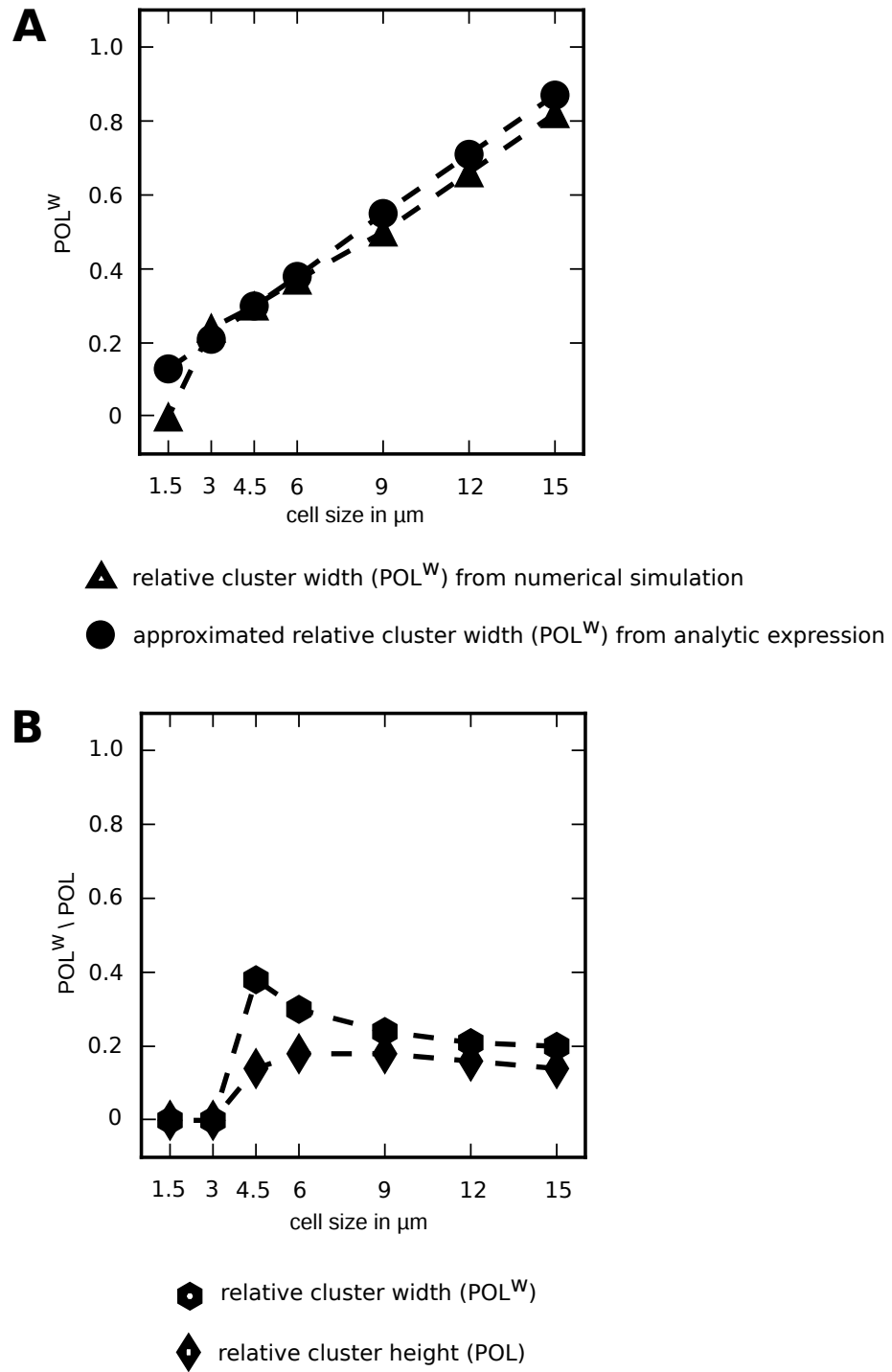


Figure S5 (A) Comparison of 2D simulations for different cell sizes and the approximation formula for the cluster width for the WP model. (B) The relative cluster width and the polarization measure POL for different cell sizes for the GOR model.

model	parameter/entity	value	unit	description
WP & GOR	u	-	$\mu M \cdot \mu m$	concentration of membrane-bound species
	v	-	μM	concentration of the cytosolic species
	$f(u, v)$	-	$\mu M \cdot \mu m s^{-1}$	flux/source term
WP	k_0	0.067	$\mu m \cdot s^{-1}$	rate of basal activation
	δ	1	s^{-1}	rate of basal dissociation
	γ	1	s^{-1}	maximal rate of auto-activation of u
	K	1	$\mu M \cdot \mu m \cdot s^{-1}$	concentration of u resulting in half-maximal rate of auto-activation
GOR	E_c	1.0	$\mu M \cdot \mu m$	membrane-bound Cdc24-Bem1 complex
	α	0.0033	$\mu M^{-3} \mu m^{-2} s^{-1}$	cooperative positive feedback
	β	0.0067	$\mu M^{-2} \mu m^{-1} s^{-1}$	noncooperative binding to membrane
	γ	0.017	s^{-1}	rate of basal dissociation from membrane

Table S1 Parameters and units used for the GOR and WP model.

REFERENCES

- [1] S. J. Altschuler, S. B. Angenent, Y. Wang, and L. F. Wu. On the spontaneous emergence of cell polarity. *Nature*, 454(7206):886–9, Aug. 2008.
- [2] C. Bakal, J. Aach, G. Church, and N. Perrimon. Quantitative morphological signatures define local signaling networks regulating cell morphology. *Science*, 316(5832):1753–6, June 2007.
- [3] P. Bastian, M. Blatt, A. Dedner, C. Engwer, R. Klöforn, R. Kornhuber, M. Ohlberger, and O. Sander. A generic grid interface for parallel and adaptive scientific computing. Part II: implementation and tests in DUNE. *Computing*, 82(2-3):121–138, 2008.
- [4] P. Bastian, M. Blatt, A. Dedner, C. Engwer, R. Klöforn, M. Ohlberger, and O. Sander. A generic grid interface for parallel and adaptive scientific computing. Part I: abstract framework. *Computing*, 82(2-3):103–119, 2008.
- [5] B. Binder, A. Goede, N. Berndt, and H.-G. Holzhütter. A conceptual mathematical model of the dynamic self-organisation of distinct cellular organelles. *PLoS ONE*, 4(12):e8295, 2009.
- [6] D. Braess. *Finite Elements: Theory, Fast Solvers, and Applications in Solid Mechanics, Third edition*. Cambridge University Press, 2007.
- [7] G. C. Brown and B. N. Kholodenko. Spatial gradients of cellular phospho-proteins. *FEBS Lett.*, 457(3):452–4, Sept. 1999.
- [8] F. Caudron and Y. Barral. Septins and the lateral compartmentalization of eukaryotic membranes. *Dev. Cell*, 16(4):493–506, Apr. 2009.
- [9] C.-S. Chou, N. Qing, and Y. Tau-Mu. Modeling Robustness Tradeoffs in Yeast Cell Polarization Induced by Spatial Gradients. *PLoS ONE*, 3(9):e3103, 09 2008.
- [10] P. G. Ciarlet. *Finite Element Method for Elliptic Problems*. Society for Industrial and Applied Mathematics, Philadelphia, PA, USA, 2002.
- [11] M. W. Covert, I. Famili, and B. O. Palsson. Identifying constraints that govern cell behavior: a key to converting conceptual to computational models in biology? *Biotechnol. Bioeng.*, 84(7):763–72, Dec. 2003.
- [12] A. E. Cowan, I. I. Moraru, J. C. Schaff, B. M. Slepchenko, and L. M. Loew. Spatial modeling of cell signaling networks. *Methods Cell Biol*, 110:195–221, 2012.
- [13] G. Dziuk. Finite Elements for the Beltrami operator on arbitrary surfaces. In *Partial Differential Equations and Calculus of Variations*, volume 1357 of *Lecture Notes in Mathematics*, pages 142–155. Springer, 1988.
- [14] G. Dziuk and C. Elliott. Surface Finite Elements for Parabolic Equations. *Journal of Computational Mathematics*, 25(4):385–407, 2007.
- [15] C. M. Elliott and T. Ranner. Finite element analysis for a coupled bulk–surface partial differential equation. *IMA Journal of Numerical Analysis*, 2012.
- [16] C. M. Elliott and T. Ranner. Finite element analysis for a coupled bulk–surface partial differential equation. *IMA Journal of Numerical Analysis*, 2012.
- [17] R. J. Ellis. Macromolecular crowding: an important but neglected aspect of the intracellular environment. *Curr. Opin. Struct. Biol.*, 11(1):114–119, Feb. 2001.

- [18] C. Engwer and S. Westerheide. Heterogenous coupling for implicitly described domains. In *Proceedings of the Domain Decomposition 21*, 2013. in press.
- [19] T. Freisinger, B. Klünder, J. Johnson, N. Müller, G. Pichler, G. Beck, M. Costanzo, C. Boone, R. A. Cerione, E. Frey, and R. Wedlich-Söldner. Establishment of a robust single axis of cell polarity by coupling multiple positive feedback loops. *Nat Commun*, 4:1807, 2013.
- [20] C. Geuzaine and J.-F. Remacle. Gmsh: A 3-D finite element mesh generator with built-in pre- and post-processing facilities. *International Journal for Numerical Methods in Engineering*, 79:1309 – 1331, 2009.
- [21] A. Goryachev and A. Pokhilko. Dynamics of Cdc42 network embodies a Turing-type mechanism of yeast cell polarity. *FEBS letters*, 582(10):1437–1443, 2008.
- [22] W. R. Holmes and L. Edelstein-Keshet. A comparison of computational models for eukaryotic cell shape and motility. *PLoS Comput. Biol.*, 8(12):e1002793, 2012.
- [23] A. Jilkine and L. Edelstein-Keshet. A comparison of mathematical models for polarization of single eukaryotic cells in response to guided cues. *PLoS computational biology*, 7(4):e1001121, Apr. 2011.
- [24] M. Kerszberg and L. Wolpert. Specifying Positional Information in the Embryo: Looking Beyond Morphogens. *Cell*, 130, july 2007.
- [25] S. Kondo and T. Miura. Reaction-Diffusion Model as a Framework for Understanding Biological Pattern Formation. *Science*, 329(1616), 2010.
- [26] T. Koto. IMEX Runge-Kutta schemes for reaction-diffusion equations. *Journal of Computational and Applied Mathematics*, 215(1):182–195, 2008.
- [27] C.-J. Ku, Y. Wang, B. Pavie, S. J. Altschuler, and L. F. Wu. On identifying information from image-based spatial polarity phenotypes in neutrophils. In *ISBI*, pages 1029–1032. IEEE, 2010.
- [28] W. Kukulski, M. Schorb, M. Kaksonen, and J. A. G. Briggs. Plasma membrane reshaping during endocytosis is revealed by time-resolved electron tomography. *Cell*, 150(3):508–20, Aug. 2012.
- [29] C. A. Larabell and K. A. Nugent. Imaging cellular architecture with X-rays. *Curr. Opin. Struct. Biol.*, 20(5):623–31, Oct. 2010.
- [30] A. Levchenko and P. A. Iglesias. Models of eukaryotic gradient sensing: Application to chemotaxis of amoebae and neutrophils. *Biophys J*, 82:50–63, 2002.
- [31] H. Levine and W. J. Rappel. Membrane-bound Turing patterns. *Physical Review E (Statistical, Nonlinear, and Soft Matter Physics)*, 72(6), 2005.
- [32] K. Luby-Phelps. Cytoarchitecture and physical properties of cytoplasm: volume, viscosity, diffusion, intracellular surface area. *Int. Rev. Cytol.*, 192:189–221, 2000.
- [33] A. F. M. Marée, V. A. Grieneisen, and L. Edelstein-Keshet. How Cells Integrate Complex Stimuli: The Effect of Feedback from Phosphoinositides and Cell Shape on Cell Polarization and Motility. *PLoS Computational Biology*, 8(3), 2012.
- [34] H. Meinhardt. Orientation of chemotactic cells and growth cones: models and mechanisms. *J. Cell. Sci.*, 112 (Pt 17):2867–74, Sept. 1999.
- [35] J. Meyers, J. Craig, and D. J. Odde. Potential for control of signaling pathways via cell size and shape. *Curr. Biol.*, 16(17):1685–93, Sept. 2006.
- [36] A. Mogilner, J. Allard, and R. Wollman. Cell polarity: quantitative modeling as a tool in cell biology. *Science*, 336(6078):175–9, Apr. 2012.
- [37] Y. Mori, A. Jilkine, and L. Edelstein-Keshet. Wave-Pinning and Cell Polarity from a Bistable Reaction-Diffusion System. *Biophysical Journal*, 94(9):3684–3697, May 2008.
- [38] Y. Mori, A. Jilkine, and L. Edelstein-Keshet. Asymptotic and Bifurcation Analysis of Wave-Pinning in a Reaction-Diffusion Model for Cell Polarization. *SIAM Journal of Applied Mathematics*, 71(4):1401–1427, 2011.
- [39] J. Muñoz-García, Z. Neufeld, and B. N. Kholodenko. Positional Information Generated by Spatially Distributed Signaling Cascades. *PLoS Computational Biology*, 5(3), 2009.
- [40] M. P. Neilson, D. M. Veltman, P. J. M. van Haastert, S. D. Webb, J. A. Mackenzie, and R. H. Insall. Chemotaxis: a feedback-based computational model robustly predicts multiple aspects of real cell behaviour. *PLoS Biol.*, 9(5):e1000618, May 2011.
- [41] I. L. Novak, F. Gao, Y.-S. Choi, D. Resasco, J. C. Schaff, and B. M. Slepchenko. Diffusion on a Curved Surface Coupled to Diffusion in the Volume: Application to Cell Biology. *J. Comput. Phys.*, 226(2):1271–1290, Oct. 2007.
- [42] S. Okada, M. Leda, J. Hanna, N. S. Savage, E. Bi, and A. B. Goryachev. Daughter Cell Identity Emerges from the Interplay of Cdc42, Septins, and Exocytosis. *Developmental Cell*, 26(2):148–161, 2013.
- [43] M. Otsuji, S. Ishihara, C. Co, K. Kaibuchi, A. Mochizuki, and S. Kuroda. A mass conserved reaction-diffusion system captures properties of cell polarity. *PLoS computational biology*, 3(6):e108, June 2007.
- [44] E. M. Ozbudak, A. Becskei, and A. van Oudenaarden. A system of counteracting feedback loops regulates Cdc42p activity during spontaneous cell polarization. *Dev. Cell*, 9(4):565–71, Oct. 2005.

- [45] A. Rätz and M. Röger. Symmetry breaking in a bulk-surface reaction-diffusion model for signaling networks. *arXiv:1305-6172*, 2013.
- [46] W. Schiesser. *The numerical method of lines*. Academic Press Inc., 1991. Integration of partial differential equations.
- [47] J. Schöneberg and F. Noé. ReaDDy—a software for particle-based reaction-diffusion dynamics in crowded cellular environments. *PLoS ONE*, 8(9):e74261, 2013.
- [48] S. J. Singer and G. L. Nicolson. The fluid mosaic model of the structure of cell membranes. *Science*, 175(4023):720–31, Feb. 1972.
- [49] K. Takahashi, S. N. V. Arjunan, and M. Tomita. Space in systems biology of signaling pathways—towards intracellular molecular crowding in silico. *FEBS Lett.*, 579(8):1783–8, Mar. 2005.
- [50] K.-E. Teigen, X. Li, J. Lowengrub, F. Wang, and A. Voigt. A diffuse-interface approach for modeling transport, diffusion and adsorption/desorption of material quantities on a deformable interface. *Communications in mathematical sciences*, 4(7):1009–1037, Dec. 2009.
- [51] G. Vereb, J. Szöllosi, J. Matkó, P. Nagy, T. Farkas, L. M. L. W. T. A. Vigh, and S. Damjanovich. Dynamic, yet structured: The cell membrane three decades after the Singer-Nicolson model. *Proc. Natl. Acad. Sci. U.S.A.*, 100(14):8053–8, July 2003.
- [52] G. R. Walther, A. F. M. Marée, L. Edelstein-Keshet, and V. A. Grieneisen. Deterministic versus stochastic cell polarisation through wave-pinning. *Bull. Math. Biol.*, 74(11):2570–99, Nov. 2012.
- [53] D. Wei, S. Jacobs, S. Modla, S. Zhang, C. L. Young, R. Cirino, J. Caplan, and K. Czymmek. High-resolution three-dimensional reconstruction of a whole yeast cell using focused-ion beam scanning electron microscopy. *BioTechniques*, 53(1):41–8, July 2012.
- [54] D. Wei, S. Jacobs, S. Modla, S. Zhang, C. L. Young, R. Cirino, J. Caplan, and K. Czymmek. High-resolution three-dimensional reconstruction of a whole yeast cell using focused-ion beam scanning electron microscopy. *BioTechniques*, 53(1):41–8, July 2012.
- [55] J. Wloka. *Partial Differential Equations*. Cambridge University Press, 1987.